日本磁気学会
ISSN 1882-2924
Journal of the Magnetics Society of Japan
Electronic Journal URL: https://www.jstage.jst.go.jp/browse/msjmag

Vol.40 No.2 2016

Journal

INDEX

JOURNAL OF THE MAGNETICS SOCIETY OF JAPAN

Vol.40 No.2 2016

日本磁気学会

ISSN 1882-2924

HP: http://www.magnetics.jp/ e-mail: msj@bj.wakwak.com

Electronic Journal: http://www.jstage.jst.go.jp/browse/msjmag

Journal of the Magnetics Society of Japan

Vol. 40, No. 2

Electronic Journal URL: https://www.jstage.jst.go.jp/browse/msjmag

CONTENTS

J. Magn. Soc. Jpn., **40**, 19-21 (2016) <Letter>

Negative Hypothesis of Equivalence between Dynamic Magnetic Loss and Eddy Current Loss in Ferrite Grains

H. Saotome

Faculty of Engineering, Chiba University, *1-33 Yayoi-cho, Inage-ku, Chiba 263-8522, Japan*

The *B-H* loop of ferrites consists of two areas: one is the DC hysteresis loop and the other corresponds to the dynamic magnetic loss. The former is temperature dependent whereas the latter is temperature independent. The difference in the temperature dependence of these two areas suggests that the physical mechanism for the dynamic magnetic loss is different than that of the DC hysteresis loss. The eddy current loss in ferrite grains is a candidate for the dynamic magnetic loss. The conductivity of the ferrite grain was estimated from the experimental results of the dynamic magnetic loss. Based on the results, it was found that the conductivity is too large for iron oxide. This fact leads to some important suggestions.

Key words: ferrite, grain, eddy current loss, iron loss, dynamic magnetic loss, temperature

1. Introduction

The DC hysteresis loss is interpreted as the energy loss caused by the damping torque of the magnetization vector in a magnetic material. The damping torque is phenomenally expressed in the second term of the Landau-Lifshitz-Gilbert (LLG) equation [1]. The DC hysteresis loss, called simply the hysteresis loss in this paper because it occurs with the time derivative of the magnetic induction, $\mathrm{d}B/\mathrm{d}t$, generally depends on temperature, and ferrites also have the same property [2]. However, it has been experimentally demonstrated that the dynamic magnetic loss in ferrites is independent of temperature [3]. Accordingly, the generation mechanism of the dynamic magnetic loss is presumed to be different from that of the hysteresis loss.

In this paper, it is assumed that the dynamic magnetic loss is caused by the eddy current in ferrite grains, and the conductivity of the grains is estimated to match the experimental and computational losses. This assumption is examined based on the obtained conductivity and the result of the examination gives some novel suggestions for the LLG equation and improving ferrite property.

2. Dynamic magnetic loss

Exciting a ferrite core at a high frequency yields the *B-H* loop shown as a solid line in Fig. 1. The hysteresis loop is shown as a broken line in the same figure. The hysteresis loop of ferrites does not shrink at frequencies lower than certain values, such as 1 kHz. The magnetic field intensity of the *B-H* loop is divided into two components:

$$H = H_\mathrm{d} + H_\mathrm{f}, \tag{1}$$

where H_f increases with the exciting frequency, i.e., $\mathrm{d}B/\mathrm{d}t$. The average dynamic magnetic loss, $\bar{p}_\mathrm{f}$ (W/m^3), per period is obtained by subtracting the area of the hysteresis loop from that of the *B-H* loop, i.e.:

$$\bar{p}_\mathrm{f} = \oint_C H_\mathrm{f} \cdot \mathrm{d}B \times f, \tag{2}$$

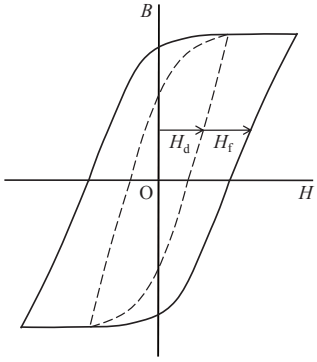

Fig. 1 *B-H* loop.

where f denotes the exciting frequency.

The *B-H* characteristics can be expressed as

$$H = \frac{1}{\mu}B + \frac{1}{\lambda_\mathrm{h}}\frac{\mathrm{d}B}{\mathrm{d}t} + \frac{1}{\lambda_\mathrm{f}}\frac{\mathrm{d}B}{\mathrm{d}t}, \tag{3}$$

where μ, λ_h and λ_f are the permeability, the hysteresis and dynamic magnetic loss parameters, respectively [4]. The hysteresis characteristics are expressed as

$$H_\mathrm{d} = \frac{1}{\mu}B + \frac{1}{\lambda_\mathrm{h}}\frac{\mathrm{d}B}{\mathrm{d}t}, \tag{4}$$

where μ depends on B for the magnetic saturation and λ_h varies to equalize the right-hand side of (4) with the measured value of H_d. The third term on the right-hand side of (3) corresponds to H_f, which is shown in Fig. 1, and is given by

$$H_\mathrm{f} = \frac{1}{\lambda_\mathrm{f}}\frac{\mathrm{d}B}{\mathrm{d}t}. \tag{5}$$

H_f increases with increasing $\mathrm{d}B/\mathrm{d}t$ when the ferrite core is excited by rectangular waveform voltages of different amplitudes proportional to $\mathrm{d}B/\mathrm{d}t$. The dynamic magnetic loss parameter, λ_f, is obtained as

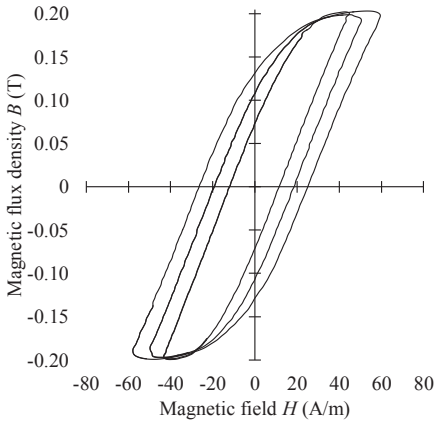

Fig. 2 Experimentally obtained *B*-*H* loops at d*B*/d*t* = 300, 600 and 900 (mT/μs), respectively. (B_m = 200 mT).

Table 1 Measured dynamic magnetic loss and corresponding conductivity in ferrite grain.

dB/dt (mT/μs)	H_f (A/m)	p_f (MW/m³)	$\bar{p}_f$ (MW/m³)	σ (S/m)
300	16	4.8	2.6	7.1×10^6
600	29	17	10	6.3×10^6
900	35	32	23	5.2×10^6

$$\lambda_f = \frac{dB}{dt}/H_f \tag{6}$$

based on the measured values of H_f and dB/dt. The measurements are carried out with rectangular waveform voltages because λ_f can be simply determined as a function of dB/dt. H_f depends on the magnetic flux density *B*, as shown in Fig. 1, indicating that λ_f is a function of *B* as well.

Multiplying H_f by dB/dt gives the instantaneous dynamic magnetic loss, p_f (W/m³).

$$p_f = H_f\left(\frac{dB}{dt}\right) = \frac{1}{\lambda_f}\left(\frac{dB}{dt}\right)^2 \tag{7}$$

The values of p_f and $\bar{p}_f$ computed from the experimentally obtained *B*-*H* loops shown in Fig. 2 for ferrite PC40 excited by rectangular waveform voltages are listed in Table 1 [3]. In the experiments, we set the maximum flux density B_m to 200 mT and dB/dt to 300, 600 and 900 mT/μs. The values of H_f and p_f listed in Table 1 are the instantaneous values at 200 mT.

3. Eddy current loss in a ferrite grain

Ferrite is composed of grains and grain boundaries. The grains are both magnetic and conductive. The grain boundaries are so highly resistive that the eddy current flowing through them is negligible. Conversely, it is conceivable that eddy currents flow inside the grains, producing the Joule heat that corresponds to the dynamic magnetic loss.

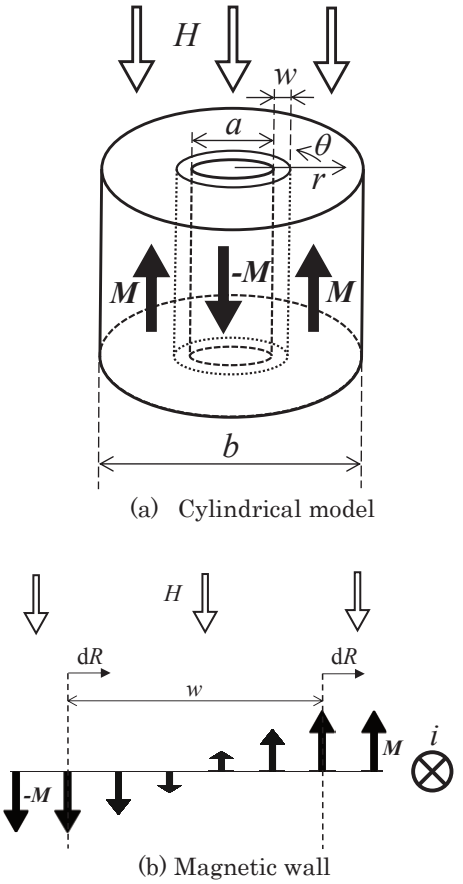

Fig. 3 Estimation of the eddy current loss in a ferrite grain.

To analyze the eddy current loss in a ferrite grain, a cylindrical grain model is assumed, as shown in Fig. 3(a), where *b* designates the diameter of a grain [1]. *H*, ***M*** and *w* are the magnetic field applied by an exciting current flowing in the winding of the core, the magnetization vector in the grain and the width of the magnetic wall, respectively. *w* is assumed to be significantly smaller than *a* and *b* shown in Fig. 3(a). In the magnetic wall, the directions of the magnetization vectors change continuously, as shown in Fig. 3(b). The direction of the magnetization vector also changes dynamically with changes in *H*; as a result, the magnetic wall moves to increase the magnetization vector that is in the same direction as *H*.

When *H* increases, the eddy current, *i*, flows in the positive θ direction in the area where $r = a/2$ to $b/2$ and increases, because of the magnetic wall movement. dH/dt occurs in the areas not only where $r = a/2$ to $b/2$, but also inside *a*; however the electric field yielded by $\mu_0\, dH/dt$ is negligibly small compared to that generated by the movement of the magnetic wall; therefore, the eddy current caused directly by $\mu_0\, dH/dt$ is ignored.

The net magnetic field intensity applied to the magnetization vectors in the magnetic wall is given by

$$H_d = H - H_f, \tag{8}$$

where $-H_f$ is caused by i. H_d generates the torque on the magnetization vectors. The rotations of the magnetization vectors are damping and result in the hysteresis loss. The power loss expressed in (7) with respect to H_f, corresponds to the eddy current loss in the grain.

The average eddy current loss density in a ferrite grain, p (W/m^3), is calculated with the conductivity σ of the grain as follows[1]. As H increases, the magnetic wall moves outward with at a rate of $\mathrm{d}R/\mathrm{d}t$, as shown in Fig. 3(b). Accordingly, the electro-motive force in the area where $r = a/2$ to $b/2$ is in proportion to the areal velocity of the movement and is given by

$$2\pi r E = M 2\pi \left(\frac{a}{2}\right)\frac{\mathrm{d}R}{\mathrm{d}t}, \tag{9}$$

where E is the electric field intensity and $M = |\boldsymbol{M}|$. The average eddy current loss density, p, is given by

$$p = \frac{\int_{\frac{a}{2}}^{\frac{b}{2}} \sigma E^2 \cdot 2\pi r \,\mathrm{d}r}{\pi\left(\frac{b}{2}\right)^2}. \tag{10}$$

Substituting E from (9) into (10) gives

$$p = \frac{8\sigma M^2 \left(\frac{a}{2}\right)^2}{b^2}\left(\frac{\mathrm{d}R}{\mathrm{d}t}\right)^2 \ln\frac{b}{a}. \tag{11}$$

Assuming $\mu_0 H << M$, the average $\mathrm{d}B/\mathrm{d}t$ in the grain model shown in Fig. 3(a) is expressed with respect to the electro-motive force of (9) as

$$\frac{\mathrm{d}B}{\mathrm{d}t} = \frac{M 2\pi \frac{a}{2}\frac{\mathrm{d}R}{\mathrm{d}t}}{\pi\left(\frac{b}{2}\right)^2} = \frac{8M}{b^2}\frac{a}{2}\frac{\mathrm{d}R}{\mathrm{d}t}, \tag{12}$$

which yields p as

$$p = \frac{\sigma b^2}{8}\left(\frac{\mathrm{d}B}{\mathrm{d}t}\right)^2 \ln\frac{b}{a}, \tag{13}$$

where a depends on B as shown in the following.

Assuming b = 10 (μm) for a ferrite grain, σ can be estimated from (13) and the experimental data as follows. The saturation magnetic flux density of ferrite PC40 at room temperature is 500 mT[2]; therefore, 200 mT corresponds to $a = \sqrt{0.3}\,b \cong 5.5$ (μm) which is obtained from

$$200\,(\mathrm{mT}) = 2 \times 500\,(\mathrm{mT}) \times \left\{\frac{1}{2} - \frac{\pi\left(\frac{a}{2}\right)^2}{\pi\left(\frac{b}{2}\right)^2}\right\}. \tag{14}$$

Substituting the values of $\mathrm{d}B/\mathrm{d}t$, a and b into (13) gives the σ values listed in Table 1.

Considering that the conductivity of iron is approximately 10×10^6 S/m, the values of σ listed in Table 1 are too large to correspond to the conductivity of ferrite grains, i.e., iron oxide. The conductivity of a ferrite grain of PC40 was estimated to be 10 S/m by an experiment where a high frequency of more than 10 MHz was applied directly to a ferrite core to short grain boundaries.

Table 2 Measured dynamic magnetic loss and corresponding conductivity in Ni-Zn ferrite grain.

$\mathrm{d}B/\mathrm{d}t$ (mT/μs)	H_f (A/m)	p_f (MW/m^3)	$\bar{p}_f$ (MW/m^3)	σ (S/m)
300	38	12	5.1	15×10^6
400	56	22	9.0	16×10^6
500	68	34	14	16×10^6

For a Ni-Zn core whose saturation magnetic flux density was 400 mT[3], similar estimation to Table 1 was carried out and its results were listed in Table 2 where B_m was 200 mT. It is shown that the values of σ listed in Table 2 are too large as well.

4. Conclusions

The physical mechanism of the dynamic magnetic loss is assumed to be different from that of the hysteresis loss because the former is temperature independent while the latter is temperature dependent. The estimation of the eddy current loss in a ferrite grain was carried out, and a trial to prove that the dynamic magnetic loss corresponds with the eddy current loss failed. This failure suggests the followings:

(1) The dynamic magnetic loss is assumed to be caused by the damping torque on the magnetization vector, similar to the hysteresis loss. However the temperature dependence of the two losses are different, indicating that the damping torque phenomenon for the dynamic magnetic loss should be expressed by a different term in the LLG equation, such as an additional third term that is independent of temperature.

(2) The eddy current losses in grains of actually manufactured ferrites are small enough to allow the grains to enlarge, thus improving the magnetic properties of ferrites.

References

1) S. Chikazumi: Physics of Ferromagnetism, Vol. II, - Magnetic Characteristics and Engineering Application -, (in Japanese), (Syokabo,Tokyo,1984).
2) http://product.tdk.com/ja/catalog/datasheets/ferrite_mn-zn_material_characteristics_ja.pdf
3) H. Saotome and H. Ohta: *J. Magn. Soc. Jpn.* **39**, 62(2015).
4) H. Saotome and Y. Sakaki: *IEEE Trans. Magn.*, **33**, 728 (1997).

Received Aug. 25, 2015; Revised Oct., 26, 2015; Accepted Dec. 4, 2015

J. Magn. Soc. Jpn., **40**, 22-27 (2016) <Paper>

Increase in AC-Field Frequency and Recording Performance in Microwave-Assisted Magnetic Recording

R. Koga[1], F. Akagi[1], and K. Yoshida[2]

[1]Graduate School of Electrical Engineering and Electronics, Kogakuin Univ., *1-24-2 Nishisinjuku, Shinjuku-ku, Tokyo, 163-8877 Japan*

[2] Kogakuin Univ., *1-24-2 Nishisinjuku, Shinjuku-ku, Tokyo, 163-8877 Japan*

Magnetic recording of a hard disk drive is negatively affected by a trilemma of noise, thermal fluctuation, and writability, which prevents high recording density. Microwave-assisted magnetic recording (MAMR) is a promising recording method for solving this trilemma. In this study, methods for increasing the AC-field frequency generated from a field generation layer (FGL) and recording performance were investigated using a micromagnetic simulator in consideration of magnetic interactions of an MAMR system. Firstly, we discuss methods for increasing the frequency of the AC-field by changing saturation magnetization (M_s) of the FGL. When the M_s of the FGL decreased, the AC-field amplitude decreased and its frequency increased. When the M_s of the FGL was lower than 1.4 T, the frequency was larger than 20 GHz. Secondly, we discuss the recording performances. As a result, to improve recording performance, high frequency of AC-field (> 20 GHz) is more important than the strength of STO field.

Key words: magnetic recording, microwave-assisted recording, micromagnetic simulation, spin-torque oscillator.

1. Introduction

Hard disk drives (HDDs) have been investigated to increase their areal recording density. Recently, however, HDDs have been having simultaneous problems with noise, thermal fluctuation, and writability, commonly known as a trilemma. Microwave-assisted magnetic recording (MAMR) is a promising recording method for solving this trilemma [1-10]. In MAMR, a spin torque oscillator (STO) is placed between a conventional write head and a trailing shield. Because the AC-field generated from the field generation layer (FGL) in the STO decreases the switching magnetic fields of the medium, writability can be improved. As a result, the trilemma can be solved. Toshiba demonstrated MAMR read/write system by simulation in 2013 and experimentally demonstrated the write resolution improvement by magnetization flipped type STO in 2014[9,10]. HGST experimentally demonstrated MAMR gain and read/write performance in 2015[11]. Generally speaking, high frequency and large amplitude for the AC-field are necessary to improve writability. However, performances of STO placed in the write head were poorly understood. The previous paper discussed the STO thickness and magnetic properties for obtaining the strong AC-field. However the frequency was less than 15 GHz[12,13].

In this study, we examined methods to increase the frequency of the AC-field and recording performance using a micromagnetic simulator that takes into account magnetic interactions between the write head, medium, and STO. As a result, when the M_s of the FGL was lower than 1.4 T, the frequency was larger than 20 GHz. To improve recording performance, high frequency of AC-field (> 20 GHz) is more important than the strength of STO field.

2. Calculation model

Fig. 1 shows the calculation model. The write head consists of a single-pole-type (SPT) head, including a main pole (MP), return pole (RP), and a trailing shield (TS). The medium consists of a soft recording layer, hard recording layer, nonmagnetic layer, and a soft under layer (SUL) and is called an exchange coupled composite (ECC) medium. The STO consists of an FGL and a spin injection layer (SIL). The head and medium was divided into 10-nm rectangular prism cells. A cell of the medium was assumed to be one grain. The STO was divided into 2.5-nm rectangular prism cells. Magnetization dynamic behavior was then calculated using a modified Landau-Lifshitz-Gilbert (LLG) equation with spin torque field (H_{st}), as shown below[6].

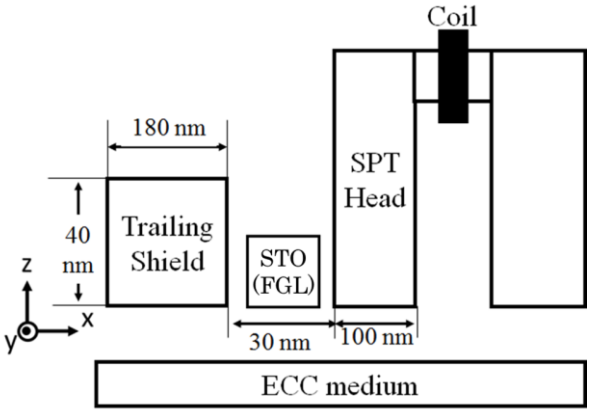

Fig. 1. Calculation model.

$$(1+\alpha^2)\frac{d\boldsymbol{M}}{dt} = -\gamma\,\boldsymbol{M}\times(\boldsymbol{H}_{eff} - \alpha\,\boldsymbol{H}_{st}) - \frac{\gamma}{M_S}\boldsymbol{M}\times\{\boldsymbol{M}\times(\alpha\,\boldsymbol{H}_{eff} + \boldsymbol{H}_{st})\} \quad (1)$$

Here, $\boldsymbol{M}$ is the magnetization vector, $\boldsymbol{H}_{eff}$ is the effective field vector, α is the damping constant, γ is the gyro magnetic constant, and M_s is the saturation magnetization. The SIL was excluded from the calculation model in this study. However, the H_{st} injected from the SIL to FGL was calculated using the following equation.

$$\boldsymbol{H}_{st} = a_j \boldsymbol{M}_p = \frac{\hbar \eta J}{2eM_{sF}d} \boldsymbol{M}_p , \quad (2)$$

where a_j is the magnitude of the spin torque field vector, $\boldsymbol{M_p}$ is the direction vector of $\boldsymbol{H_{st}}$, $\hbar$ is Planck's constant divided by 2π, η is the spin polarizability (0.5 in this study), J is the inject current density, e is the elementary charge, M_{sF} is the saturation magnetization of the FGL, and d is the FGL thickness. Tables 1-4 show the dimensions and magnetic characteristics of head, medium, and FGL. The current in the coil was 0.18 A. As shown in Fig. 2, the coil current waveform was trapezoidal with a rise time of 0.2 ns and a cycle of 2.0 ns, corresponding to a bit length of 20 nm with the relative velocity between head and medium of 20 m/s. The spacing between the air bearing surface (ABS) and the medium surface was 5 nm. In this simulator, magnetic interactions between the write head, medium, and STO were taken into account. For instance, the AC-field was generated by the precession of the magnetization of the FGL. Basically, the precession occurs due to the balance between the external field (the head-field and stray field from the medium) and the H_{st} in the perpendicular direction (x component in Fig. 1). However, in actuality, the FGL is affected not only by the x component but also by the y and z components of the external fields. This simulator takes into account all field components and can accurately simulate the processes. Thermal fluctuation was not considered.

Table 1 Magnetic characteristics of Head.

Symbol	Quantity	Value
M_s	Saturation magnetization	2.5 T
K_u	Magnetic anisotropy	3.0×10^3 J/m^3
A	Exchange stiffness constant	1.0×10^{-11} J/m

Table 2 Magnetic characteristics of FGL.

Symbol	Quantity	Value
K_u	Magnetic anisotropy	5.0×10^3 J/m^3
$A_{//}$	Exchange stiffness constant	2.0×10^{-11} J/m

Table 3 Dimensions of head, medium, and FGL.

		Quantity	Value [nm]
SPT Head	MP	Thickness	100
		Width	70
		Throat height	50
	TS	Thickness	180
		Width	540
		Height	100
	RP	Thickness	220
		Width	1000
		Height	400
Recording Medium thickness		Recording layer	10
		SUL	50
		Nonmagnetic layer	5
FGL		Width (y dir.)	30
		Height (z dir.)	30
		Thickness (x dir.)	20
Spacing between MP and FGL			5
Spacing between TS and FGL			5

Table 4 Magnetic characteristics of recording layer.

Symbol	Quantity	Value
M_s	Saturation magnetization	0.8 T
K_u	Magnetic anisotropy of soft layer	3.0×10^3 J/m^3
K_u	Magnetic anisotropy of hard layer	1.3×10^6 J/m^3
$A_{//}$	Exchange stiffness constant in plane	2.0×10^{-11} J/m
A	Exchange stiffness constant in vertical	1.0×10^{-11} J/m

Table 5 Magnetic characteristics of SUL.

Symbol	Quantity	Value
M_s	Saturation magnetization	1.5 T
K_u	Magnetic anisotropy	3.0×10^3 J/m^3
$A_{//}$	Exchange stiffness constant in plane	1.0×10^{-11} J/m
A	Exchange stiffness constant in vertical	1.0×10^{-11} J/m

3. Methods for increasing frequency of AC-field

In this chapter, we discuss methods for increasing the frequency of the AC-field. Fig. 2 shows an example of the averaged AC-field in the cross-track direction (H_y) at 9 nm under the FGL. The averaged amplitude ($<H_y>$) and frequency (f_{STO}) were evaluated. In this graph, circles from 0.5 to 1.0 ns and from 1.5 to 2.0 ns show sampling points to evaluate $<H_y>$ and f_{STO} because the AC-field was disordered at the other times due to ununiformity of the gap field during current reversal. Fig. 3 shows the M_s of the FGL dependence of $<H_y>$ and f_{STO} at H_{st} of 80 kA/m. When M_s was less than 1.4 T, f_{STO} was larger than 20 GHz, and its maximum was 22.5 GHz at M_s of 1.2 T. However, $<H_y>$ decreased with decreasing M_s. When M_s set 2.0 T, $<H_y>$ was 80 kA/m. However, $<H_y>$ was only 36 kA/m at M_s of 1.2 T. Fig. 4

shows the M_s of the FGL dependence of relative variation ($\sigma H_y/\langle H_y\rangle$) at the same H_{st} in Fig. 3. When M_s was less than 1.0 T, $\sigma H_y/\langle H_y\rangle$ drastically increased. In other words, when M_s was less than 1.0 T, the AC-field waveform was disordered. Therefore, the AC-field with the frequency over 20 GHz and low $\sigma H_y/\langle H_y\rangle$ was obtained on condition that the M_s of the FGL was between 1.2 and 1.4 T. We then investigated the increasing method of $\langle H_y\rangle$ for M_s of 1.2 and 1.4 T. Fig. 5 shows the H_{st} dependence of $\langle H_y\rangle$ and f at the M_s of the FGL of 1.2 and 1.4 T. Here, H_{st} changed from 60 to 80 kA/m. An f_{STO} over 20 GHz was obtained when H_{st} was larger than 65 kA/m. For M_s of 1.2 T, $\langle H_y\rangle$ increased from 36 to 50 kA/m as H_{st} decreased from 80 to 65 kA/m. For the M_s of 1.4 T, $\langle H_y\rangle$ increased from 50 to 60 kA/m as H_{st} decreased from 80 to 65 kA/m. However, $\langle H_y\rangle$ was lower than the maximum value of 77 kA/m in Fig. 3.

4. Recording Performance

Okamoto et al. experimentally revealed the relation between switching field and AC-field[14] . According this paper, the switching field monotonically decreased with increasing the frequency and field strength up to a critical frequency depending on the field strength. However, it was difficult to obtain the AC-field with high frequency and strong field, because both have a strong interaction, as shown in the chapter 3. Then, in this chapter, we discuss the recording performances of several AC-fields investigated in the previous chapter. Table 6 and Fig. 6 show recording models. We simulated a high $\langle H_y\rangle$ model (M_s = 2.0 T, H_{st} = 80 kA/m: model A, M_s = 1.8 T, H_{st} = 80 kA/m: model B, and M_s = 1.6 T, H_{st} = 80 kA/m: model C), high frequency models (M_s = 1.4 T, H_{st} = 80 kA/m: model D, and M_s = 1.2 T, H_{st} = 80 kA/m: model E), a model with over 20 GHz and maximum$\langle H_y\rangle$ model

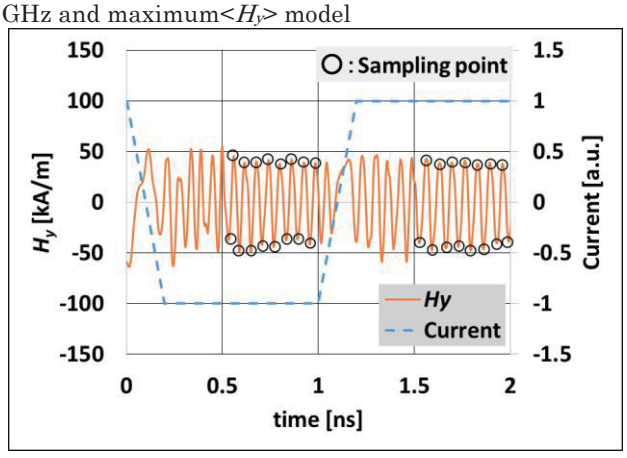

Fig. 2 Example of sampling point of y-component of AC-field (H_y) and coil current.

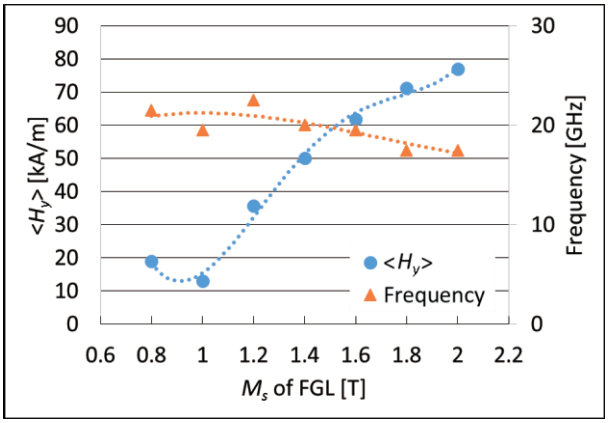

Fig. 3 Averaged y-component of AC-field $\langle H_y\rangle$ vs. M_s of FGL.

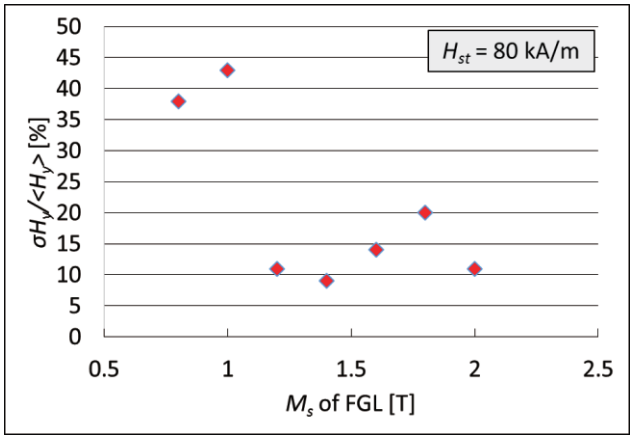

Fig. 4 Normalized variance of averaged y-component of AC-field $\sigma H_y/\langle H_y\rangle$ *vs.* M_s of FGL.

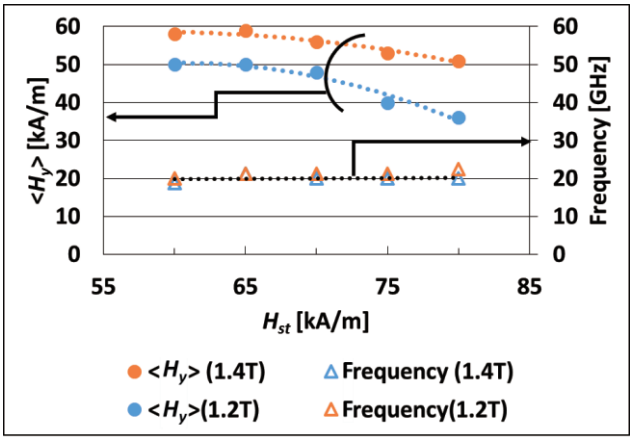

Fig. 5 Averaged y-component of AC-ield $\langle H_y\rangle$ vs. H_{st}.

(M_s = 1.4 T, H_{st} = 65 kA/m: model F), and a model without an FGL (Model G), which was a conventional write head for comparing the effects of the AC-field. The recording performances were evaluated using recording efficiency (RE), as shown in the following equation.

$$\mathrm{RE} = \frac{1}{N_{samp}} \sum_{i=1}^{Nsamp} m_{ideal}(i) \cdot m_{rec}(i) \qquad (3)$$

Here, N_{samp} is the sampling number, $m_{ideal}(i)$ is the z-component of the i-th sampling point for the ideal

magnetization pattern, and $m_{rec}(i)$ is that for the calculated pattern[8]. The RE was from −1 to 1. If the RE is 1, all magnetizations of grains are saturated and the medium is ideally recorded. Figs. 7 (a) – (g) show the recorded magnetization waveforms (z-component) from models A to G. The ideal waveform is also shown in each figure. The REs from A to G were 0.51, 0.52, 0.65 0.67, 0.83, 0.74, and 0.76, respectively. As a result, the RE of only model E was higher than that of conventional write head (model G). On the other hand, the REs of models A-D and F were lower than that of the conventional write head (model G). The $<H_y>$ values of these models were higher than that of model E, and the f_{STO}s were lower than that of model E. Figs. 8 and 9 show $<H_y>$ and f_{STO} dependence of RE, respectively. From these graphs, the REs increased with increasing f_{STO} and decreasing $<H_y>$. Therefore, the model with low $<H_y>$ and high f_{STO} showed a marked improvement in recording performance. As a result, to improve recording performance, high frequency of AC field (> 20 GHz) is more important than the strength of STO field.

Table 6 Recording FGL models.

	Model	M_s [T]	H_{st} [kA/m]	$<H_y>$ [kA/m]	f_{STO} [GHz]
A		2	80	77	17.5
B	High $<H_y>$	1.8	80	71	17.5
C		1.6	80	62	19.5
D	High	1.4	80	51	20.0
E	frequency	1.2	80	36	22.5
F	f_{STO} ≧20GHz $<H_y>_{max}$	1.4	65	60	20.0
G	Without FGL (w/o AC field)				

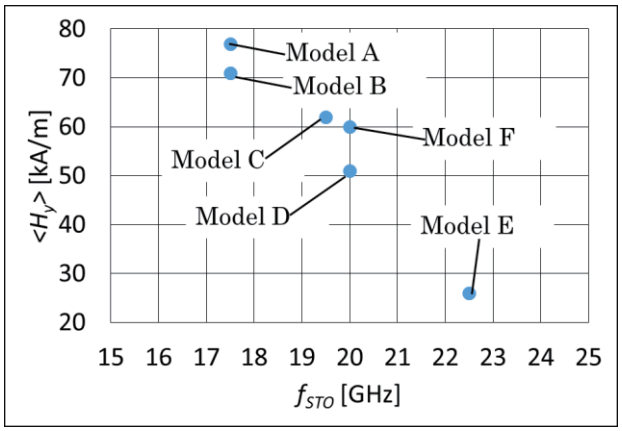

Fig. 6 Relationship diagram of averaged y-component of AC-field $<H_y>$ and frequency f_{STO} of each model.

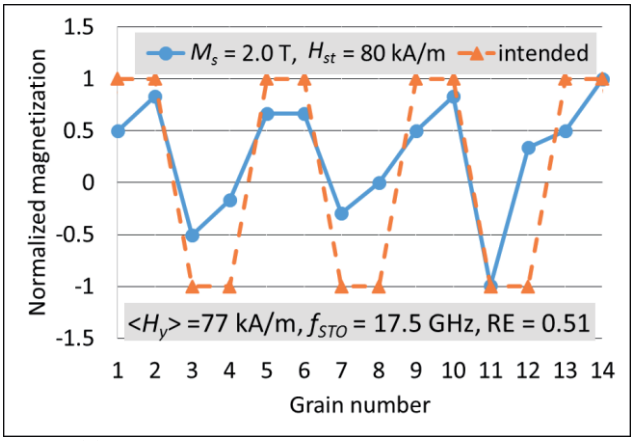

Fig. 7 (a) Recording waveform of model A.

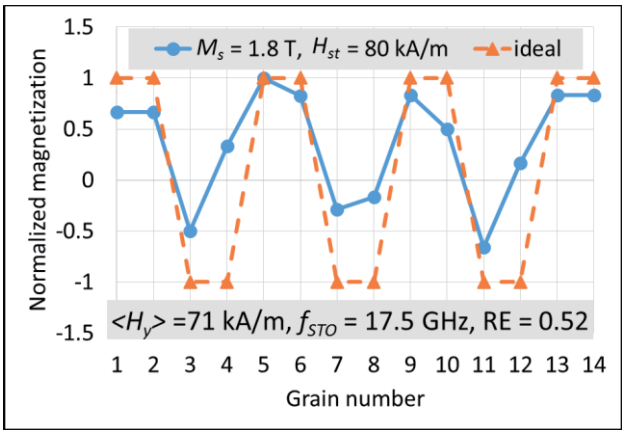

Fig. 7 (b) Recording waveform of model B.

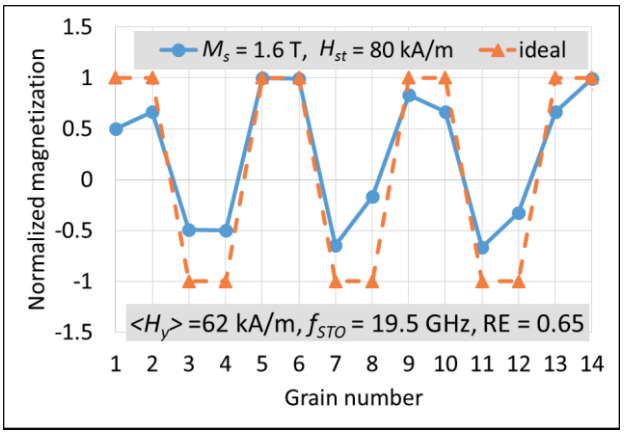

Fig. 7 (c) Recording waveform of model C.

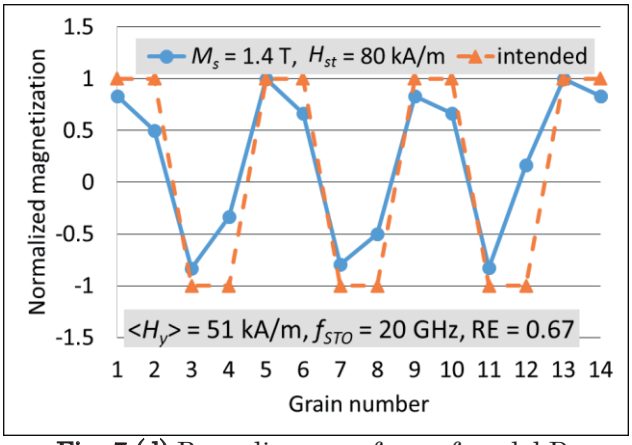

Fig. 7 (d) Recording waveform of model D.

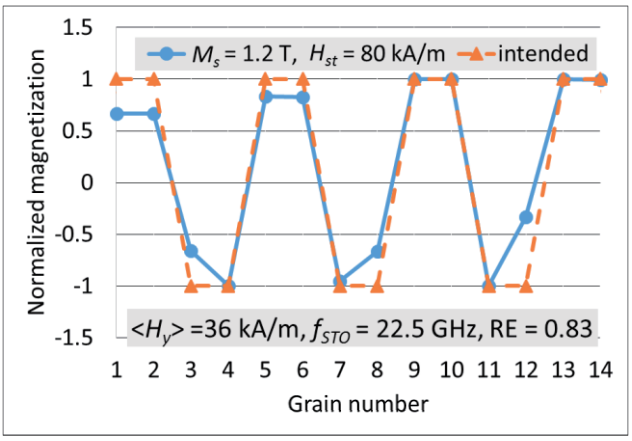

Fig. 7 (e) Recording waveform of model E.

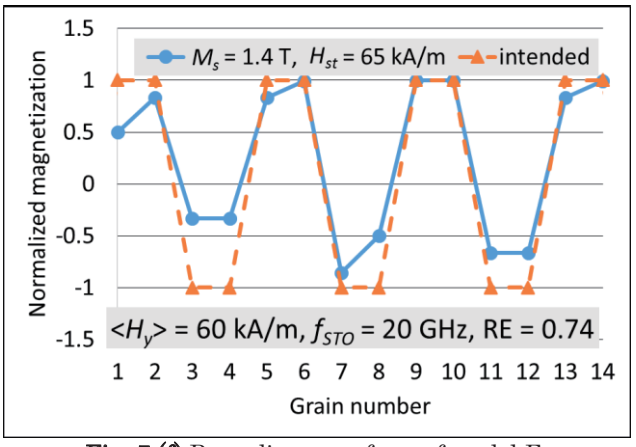

Fig. 7 (f) Recording waveform of model F.

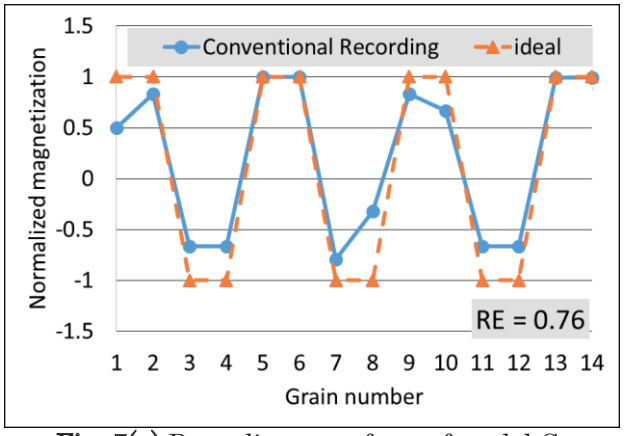

Fig. 7(g) Recording waveform of model G.

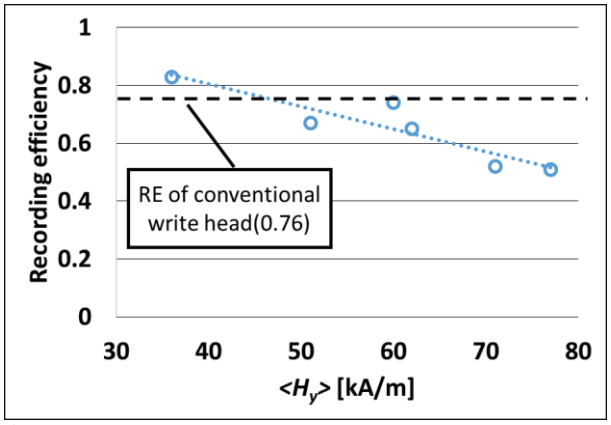

Fig. 8 Averaged y-component of STO field <H_y> vs. recording efficiency (RE).

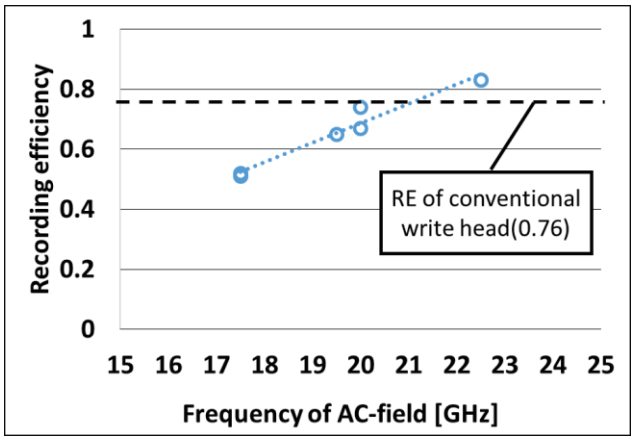

Fig. 9 Frequency of AC-field f_{STO} vs. recording efficiency (RE).

5. Conclusions

We investigated methods to increase the AC-field frequency and recording performance in microwave-assisted magnetic recording. The following results were obtained.

1. When the M_s of the FGL decreases, the AC-field amplitude decreases and its frequency of AC-field increases. When the M_s of the FGL is lower than 1.4 T, frequency is larger than 20 GHz.
2. To improve recording performance, high frequency of AC-field (> 20 GHz) is more important than the strength of STO field.

Acknowledgements This study was supported in part by the Storage Research Consortium (SRC), Japan.

References

1) Y. Tang, and J.-G. Zhu,: *IEEE Trans. Magn.*, **44**, 3376 (2008).
2) M. Shiimoto, M. Igarashi, M. Sugiyama, Y. Nishida and I. Tagawa,: *IEEE Trans. Magn.*, **49**, 3636, (2013).
3) J-G.Zhu and Y. Wang,: *IEEE Trans. Magn.*, **46**, 751, (2010).
4) M. Igarashi, K. Watanabe, Y. Hirayama and Y. Shiroishi, : *IEEE Trans. Magn.*, **48**, 3284, (2012).
5) M. Igarashi, Y. Suzuki, Y. Sato, : *IEEE Trans. Magn.*, **46**, 3738 (2013).
6) S. Asaka, T. Hashimoto, K. Yoshida and Y. Kanai, : *IEICE TRANS. ELECTRON.*, **E96-C**, 1484, (2013).
7) T. Takahashi, S. Asaka, K. Yoshida and Y. Kanai, *J. Magn. Soc. Jpn.*, **36**, 150 (2012).
8) K. Yoshida,: *IEEE Trans. on Magn.*, **50**, 3202504 (2014).
9) K. Yamada, M. Takagishi, K. Koi, A. Takeo,: Dig. TMRC2013 E1 (2013)
10) A. Takeo, G. Koizumi, N. Naita, K. Yamada, W. chen, M. Zhang, Q. Hu, M. Li, and K. Koi: Dig. Intermag2014 AD-2 (2014)
11) I. Tagawa, M. Shiimoto, M. Matsubara, S. Nosaki, J. Aoyama, and Y. Urakami,: Dig. TMRC2015, D6 (2015)
12) R. Koga, F. Akagi, K. Yoshida: *IEICE Technical Report*, **114**, 1 (2014)
13) R. Koga, F. Akagi, K. Yoshida: *IEICE TRANS. ELECTRON.*, **J98-C**, 138 (2015)
14) S. Okamoto, N. Kikuchi, M. Furuta, O. Kitakami, and T. Shimatsu,: *Phys. Rev. Lett.* **109**, 237209 (2012).

Received Aug. 25, 2015; Revised Oct. 30, 2015; Accepted Dec. 04, 2015

J. Magn. Soc. Jpn., **40**, 28-34 (2016) <Paper>

Advantages of Increasing Writing Temperature in Heat-Assisted Magnetic Recording

T. Kobayashi, Y. Isowaki, and Y. Fujiwara
Graduate School of Engineering, Mie Univ., *1577 Kurimamachiya-cho, Tsu 514-8507, Japan*

The advantages of increasing the writing temperature T_w in heat-assisted magnetic recording (HAMR) are summarized. As T_w increases, the anisotropy constant ratio, which is a new parameter we introduced, can be decreased since the anisotropy constant at the working temperature and the heat-transfer thermal gradient are increased. A relatively thin recording layer (RL) is allowable since the heat-transfer thermal gradient is reduced by increasing the RL thickness because of the adiabatic effect of the RL. Relatively large standard deviations in grain size and anisotropy are permissible since the probability of magnetization reversal is low even for small grains and grains with small anisotropy during the writing period, respectively. A relatively large standard deviation in the Curie temperature is allowable since the heat-transfer thermal gradient is increased. For Fe-Ni-Pt films, the temperature dependence of the anisotropy field is suitable for HAMR when T_w is high. All of the above are advantageous when preparing HAMR media.

Key words: heat-assisted magnetic recording, writing temperature, anisotropy constant ratio, standard deviation, temperature dependence

1. Introduction

Heat-assisted magnetic recording (HAMR) is a candidate for solving the trilemma problem[1] of magnetic recording (MR). HAMR is a recording method in which the medium is heated to reduce the coercivity during the writing period.

We have reported a design method that uses a model calculation for HAMR media[2]. In that paper, we introduced a new parameter, the anisotropy constant ratio K_u/K_{bulk}, which is the intrinsic ratio of film anisotropy constant K_u to bulk K_u. Finding a way to increase K_u/K_{bulk} is a challenging task. Therefore, it is necessary to design a medium with a smaller K_u/K_{bulk}. The dependences of K_u/K_{bulk} on the grain number per bit n, the standard deviation of the grain size σ_D, the recording layer thickness h, and the writing temperature T_w were clarified.

We have subsequently improved our design method, and many relationships between the media design parameters and K_u/K_{bulk} have been revealed[3]. The design parameters we examined were the MR method (HAMR and HAMR combined with shingled MR (SHAMR)), h, the thermal conductivity of the interlayer 1 (shown in Fig. 2), the light-spot diameter, the heat-spot diameter, the linear velocity, T_w, n, and σ_D. As a result, we found that increasing T_w is only effective for reducing K_u/K_{bulk} when we compare it with the K_u/K_{bulk} value calculated using standard parameter values.

The above-mentioned examinations were carried out by changing one parameter. Next, we provided examination results for a combination of more than two parameters[4]. In conclusion, the combinations that can reduce K_u/K_{bulk} always have SHAMR as one parameter. However, the use of SHAMR degrades the read/write performance of the hard drive. Although a lower T_w is better in terms of the heat resistance of the writing head and/or the surface lubricant, increasing T_w appears to be the only way of reducing K_u/K_{bulk} for HAMR media.

Increasing T_w has many advantages in addition to reducing K_u/K_{bulk}. In this study, we summarize the advantages of increasing T_w.

2. Calculation Conditions

The medium was assumed to be granular. The arrangement of the grains was not considered. Figure 1 (a) is a schematic illustration of the area near the writing position for HAMR. The writing field H_w is applied to a wide area including the writing position. The circle denoted by T_w is an isotherm of T_w, and d_w is the heat-spot diameter. The white regions indicate upward or downward magnetization, and the gray regions indicate the magnetization transition that contains upward and downward magnetization grains. The transition region spreads to adjacent tracks as a result of rewriting operations on the ith track.

T_{rec} is the maximum temperature[3] at which the information on the trailing side can be held during writing. Δx is the distance[3] from the position of T_w to that of T_{rec}. On the other hand, T_{adj} is the maximum temperature[3] at which the information in adjacent tracks can be held during rewriting. Δy is the distance[3] from the position of T_w to that of T_{adj}.

The bit area S is fixed, and S is the product of the bit pitch d_B and the track pitch d_T. The method for determining d_T/d_B was reported in a previous paper[2].

Figure 1 (b) shows the writing-head configuration. It was assumed that the main-pole size of the head is 600 nm (down-track direction) × 300 nm (cross-track

direction), and the writing position is located on the trailing side of the main pole. H_{adj} is the maximum head field[3] that can hold the information under the main pole during rewriting. The maximum temperature under the main pole is T_a, which is the maximum working temperature of the hard drive, and was assumed to be 330 K.

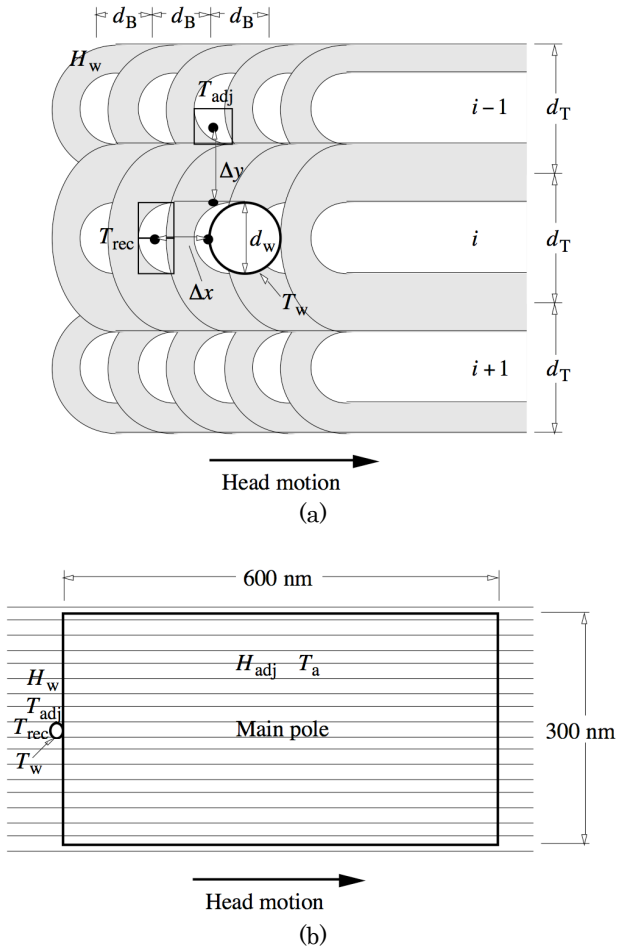

Fig. 1 Schematic illustrations of (a) writing position and (b) writing-head configuration.

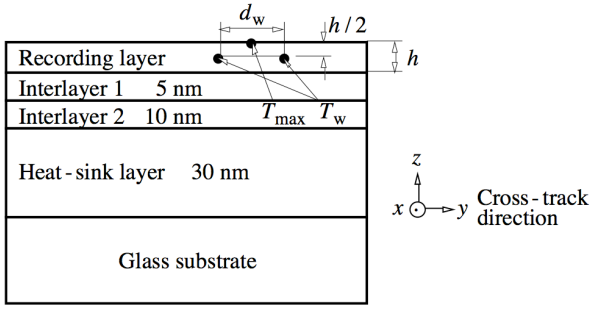

Fig. 2 Medium structure and definition of temperatures.

The standard medium structure is shown in Fig. 2. The standard medium consists of four layers, that is, a recording layer RL (Fe-Pt base, thickness h = 8 nm), an interlayer 1 IL1 (MgO base, 5 nm), an interlayer 2 IL2 (Cr base, 10 nm), and a heat-sink layer HSL (Cu base, 30 nm). The x, y, and z axes are the down-track, cross-track, and thickness directions, respectively. T_w is defined at the heat-spot edge and is at the center of the RL layer in the thickness direction. The two positions of T_w in Fig. 2 are at a distance of d_w in the cross-track direction as shown in Fig. 1 (a). T_w and d_w are the design parameters. T_w can be changed by the light power used for heating. T_{max} is defined as the maximum surface temperature.

Figure 3 (a) shows the heat-transfer thermal gradient $\partial T/\partial x$ for the down-track direction and $\partial T/\partial y$ for the cross-track direction at T_w and the center of the RL layer in the thickness direction as a function of the RL thickness h. $\partial T/\partial x$ and $\partial T/\partial y$ were calculated by a heat-transfer simulation[2], and $\partial T/\partial x \approx \partial T/\partial y$ can be seen. The dependence of T_{max} on h is shown in Fig. 3 (b).

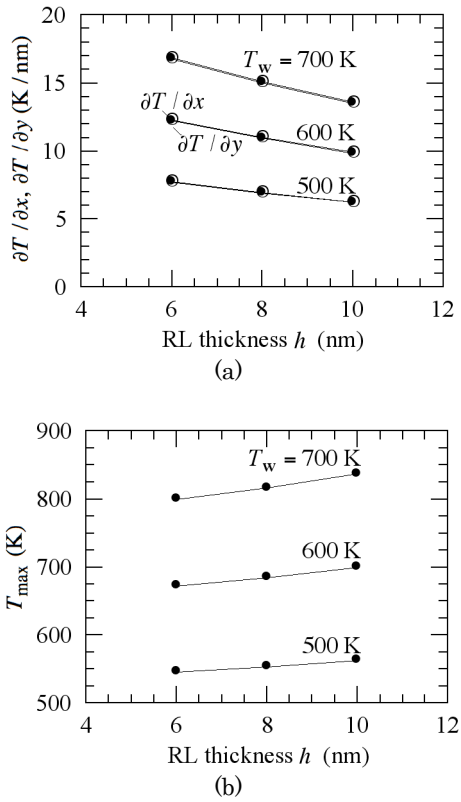

Fig. 3 (a) Heat-transfer thermal gradients $\partial T/\partial x$ for down-track direction and $\partial T/\partial y$ for cross-track direction, and (b) maximum surface temperature T_{max} as a function of RL thickness h.

The standard parameter values used for the media design are summarized in Table 1. The standard deviations of the anisotropy constant σ_K and the Curie temperature σ_{Tc} are newly introduced design parameters.

The HAMR media are designed to obtain the minimum K_u/K_{bulk} value using the procedure shown in Fig. 4. First, the design parameters and K_u/K_{bulk} = 1 are set. Four HAMR conditions (1), (2), (3), and (4) are

examined after determining the composition of the recording layer. If there are margins for all four conditions, K_u/K_{bulk} can be reduced. When one of the four conditions reaches the limit, the minimum K_u/K_{bulk} value can be determined. That condition becomes a limiting factor.

Table 1 Standard parameter values used for media design.

User areal density (Tbpsi)	4
Bit area S (nm^2)	140
Effective track width d_{ET} (nm)	10
Ambient temperature T_a (K)	330
Writing temperature T_w (K)	500
Grain number per bit n (grain / bit)	4
RL thickness h (nm)	8
Standard deviation of grain size σ_D/D_m (%)	10
Standard deviation of anisotropy σ_K/K_{um} (%)	0
Inter - grain exchange coupling J (erg / cm^2)	0
MR method	HAMR
Light - spot diameter d_L (nm)	9.0
Heat - spot diameter d_w (nm)	10
Linear velocity v (m / s)	10
Thermal conductivity of IL1 K (W / (cmK))	0.5
Standard deviation of Curie temp. σ_{Tc}/T_c (%)	0

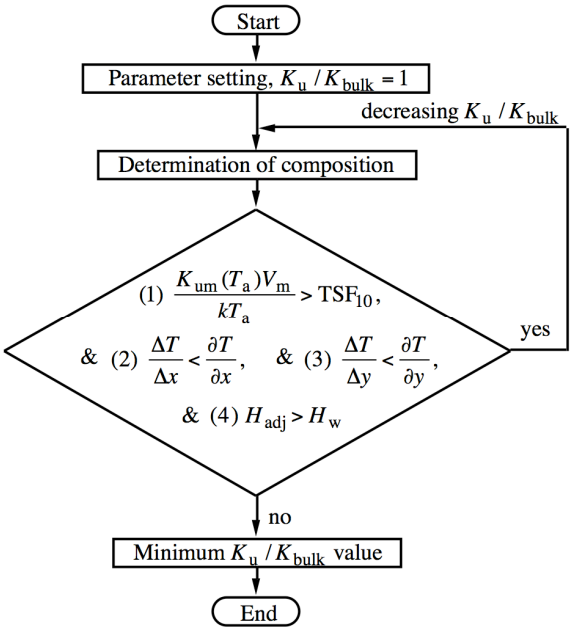

Fig. 4 HAMR media design procedure for obtaining the minimum anisotropy constant ratio K_u/K_{bulk} [3].

Condition (1), the information stability during 10 years of archiving, is expressed as

$$\frac{K_{um}(T_a)V_m}{kT_a} \geq TSF_{10}, \qquad (1)$$

where $K_{um}(T_a)V_m/kT_a$ is a medium thermal stability factor, $K_{um}(T_a)$ is the mean anisotropy constant, $V_m = D_m^2 \times h$ is the grain volume for the mean grain size D_m, k is the Boltzmann constant, and TSF_{10} is the statistical thermal stability factor during 10 years of archiving[3] calculated statistically using grain-error probability and many bits under the condition of a 10^{-3} bit error rate. The statistical thermal stability factor $TSF(\tau, n, \sigma_D, \sigma_K)$ is generally a function of the archiving period τ, the grain number per bit n, the standard deviation of the grain size σ_D, and the standard deviation of the anisotropy σ_K [5]. TSF is unrelated to K_u. And TSF_{10} means $TSF(10\ years, n, \sigma_D, \sigma_K)$.

Condition (2), the information stability on the trailing side during writing, is expressed as

$$\frac{\Delta T}{\Delta x} = \frac{T_w - T_{rec}}{\Delta x} \leq \frac{\partial T}{\partial x}, \qquad (2)$$

where $\Delta T/\Delta x$ is the medium thermal gradient for the down-track direction.

Condition (3), the information stability in adjacent tracks during rewriting, is expressed as

$$\frac{\Delta T}{\Delta y} = \frac{T_w - T_{adj}}{\Delta y} \leq \frac{\partial T}{\partial y}, \qquad (3)$$

where $\Delta T/\Delta y$ is the medium thermal gradient for the cross-track direction. $\Delta T/\Delta x$ and $\Delta T/\Delta y$ are the minimum thermal gradients required by the medium for information stability[3].

Condition (4), the information stability under the main pole during rewriting, is expressed as[3]

$$H_{adj} \geq H_w. \qquad (4)$$

Conditions (2) and (3) can be combined as

$$\frac{\Delta T}{\Delta x} = \frac{\Delta T}{\Delta y} \leq \frac{\partial T}{\partial x} = \frac{\partial T}{\partial y}, \qquad (5)$$

since $\partial T/\partial x \approx \partial T/\partial y$. Condition (4) has margins for all the cases we examined. Therefore, the major limiting factors in the media design are condition (1) given by Eq. (1) ((1) $K_{um}(T_a)V_m/kT_a \geq TSF_{10}$) and conditions (2) and (3) given by Eq. (5) (hereafter, shown as $\Delta T/\Delta x = \Delta T/\Delta y \equiv \Delta T/\Delta x(y)$, $\partial T/\partial x = \partial T/\partial y \equiv \partial T/\partial x(y)$, and (2), (3) $\Delta T/\Delta x(y) \leq \partial T/\partial x(y)$).

3. Calculation Results

3.1 Anisotropy constant ratio

The dependence of the required K_u/K_{bulk} value on T_w is shown in Table 2. We extended the calculation range up to T_w = 700 K. The Curie temperature T_c is 4 - 8 K higher than T_w. T_w is determined by the light power used for heating, and the T_c of the medium is determined by T_w. If the light power alone is increased for a medium with the same T_c, the written bits will be spread in the cross-track direction, and it becomes impossible to keep the track pitch constant. Therefore,

T_c must be increased to increase T_w. The magnetization M_s, K_{um}, the mean coercivity H_{cm}, and $K_{um}V_m/kT$ at 300 K are also shown in the table. H_{cm} was assumed to be equal to the mean anisotropy field $H_{km} = 2K_{um}/M_s$. TSF_{10} in condition (1) is constant for T_w, and $K_{um}(T_a)V_m/kT_a$ increases as T_w increases since $K_{um}(T_a)$ increases[4]. $\partial T/\partial x(y)$ in conditions (2) and (3) also increases as T_w increases[3]. The limiting factors are conditions (2) and (3). H_{adj} in condition (4) is sufficiently larger than H_w. Although K_{um}(300 K) apparently increases as T_w increases, K_u/K_{bulk} can decrease from 0.66 for T_w = 500 K to 0.45 for T_w = 700 K. The optimum d_B, d_T, and d_T/d_B values are shown in the table.

K_u/K_{bulk} is a function of the heat-transfer thermal gradient $\partial T/\partial x(y)$ as shown in Fig. 5. As $\partial T/\partial x(y)$ increases, K_u/K_{bulk} first becomes lower, and then becomes constant with respect to $\partial T/\partial x(y)$. In the range where K_u/K_{bulk} changes, the limiting factors are conditions (2) and (3) $\Delta T/\Delta x(y) \le \partial T/\partial x(y)$. And it is condition (1) $K_{um}(T_a)V_m/kT_a \ge TSF_{10}$ in the range where K_u/K_{bulk} is constant. Although increasing T_w is effective for reducing K_u/K_{bulk}, a higher $\partial T/\partial x(y)$ is needed to obtain a lower K_u/K_{bulk}. The filled circles show the K_u/K_{bulk} values and their $\partial T/\partial x(y)$ values calculated by a heat-transfer simulation. The values correspond to those in Table 2. If we can realize a greater increase in $\partial T/\partial x(y)$ by examining the media structure, we can expect to reduce K_u/K_{bulk} even further.

Table 2 Calculation results of HAMR media design for various writing temperatures T_w.

T_w (K)	500	600	700
D_m (nm)	4.92	4.92	4.92
T_c (K)	508	606	704
M_s(300 K) (emu/cm^3)	616	771	912
K_{um} (300 K) (10^6 erg/cm^3)	17	21	26
H_{cm} (300 K) = H_{km} (300 K) (kOe)	54	55	57
$K_{um}V_m/kT$ (300 K)	78	99	120
TSF_{10}	62	62	62
(1) $K_{um}(T_a)V_m/kT_a \ge TSF_{10}$	64	84	105
$\partial T/\partial x(y)$ (K/nm)	6.9	11.0	15.1
(2), (3) $\Delta T/\Delta x(y)$ (K/nm) $\le \partial T/\partial x(y)$	6.9	11.0	15.1
H_w (kOe)	9.85	12.3	14.6
(4) H_{adj} (kOe) $\ge H_w$	16.7	22.0	26.3
K_u/K_{bulk}	0.66	0.52	0.45
d_B (nm)	6.57	6.81	6.95
d_T (nm)	21.3	20.6	20.1
d_T/d_B	3.25	3.02	2.90

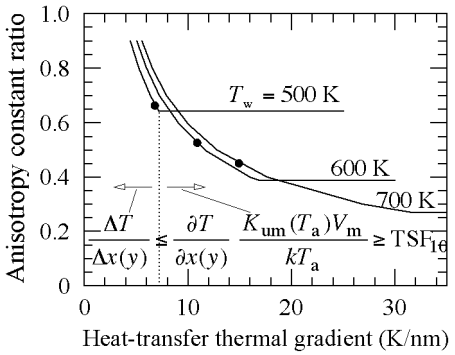

Fig. 5 Dependence of anisotropy constant ratio K_u/K_{bulk} on heat-transfer thermal gradient $\partial T/\partial x(y)$ for various writing temperatures T_w.

3.2 RL thickness

The dependence of K_u/K_{bulk} on $\partial T/\partial x(y)$ is shown in Fig. 6 where the calculation parameter is the RL thickness h. When (a) T_w = 500 K, K_u/K_{bulk}, shown by the filled circles, is increased by changing h from 8 nm to 6 nm as previously reported[4]. On the other hand, when (b) T_w = 700 K, the K_u/K_{bulk} values are almost the same for the h = 6 to 10 nm calculation range since the limiting factors become conditions (2) and (3) $\Delta T/\Delta x(y) \le \partial T/\partial x(y)$ for h = 6 nm, and $\partial T/\partial x(y)$ is reduced by increasing h due to the adiabatic effect of RL. Therefore, when T_w is high, a relatively thin RL thickness is allowable.

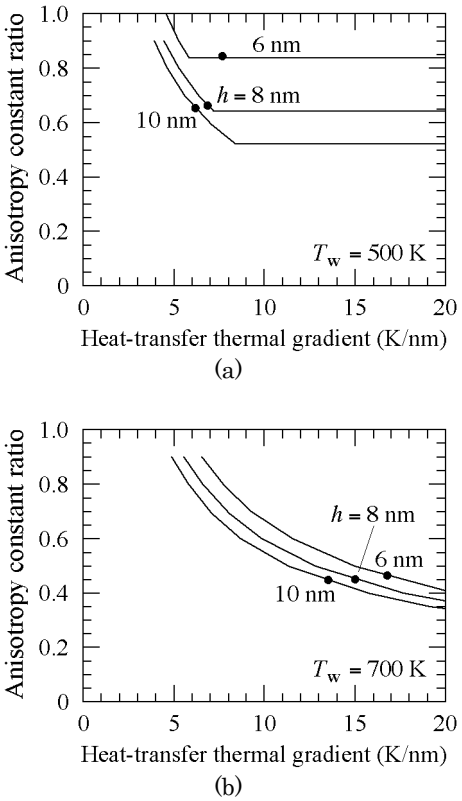

Fig. 6 Dependence of K_u/K_{bulk} on $\partial T/\partial x(y)$ at (a) T_w = 500 K[4] and (b) 700 K for various RL thicknesses h.

3.3 Standard deviation of grain size

The calculation results for the standard deviation of the grain size σ_D are shown in Fig. 7.

As σ_D increases, K_u/K_{bulk}, shown by the filled circle, is greatly increased when (a) T_w = 500 K[4]. On the other hand, when (b) T_w = 700 K, the increase in K_u/K_{bulk} caused by increasing σ_D is not great.

The limiting factor is largely (1) $K_{um}(T_a)V_m/kT_a \geq \mathrm{TSF}_{10}$ when (a) T_w = 500 K. Figure 8 shows the dependence of the statistical thermal stability factor TSF_{10} on σ_D during τ = 10 years of archiving. As σ_D increases, the number of small size grains increases, and the probability of magnetization reversal for these small size grains is high over long periods, *e.g.* τ = 10 years. Therefore, K_{um} and K_u/K_{bulk} must be increased to maintain a low bit error rate when σ_D is large.

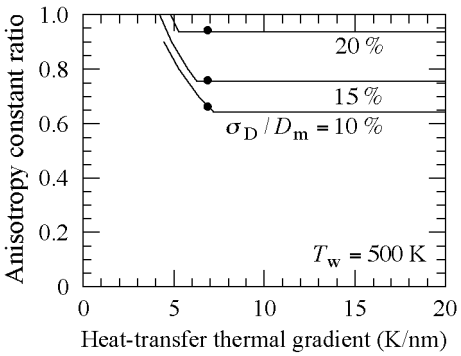

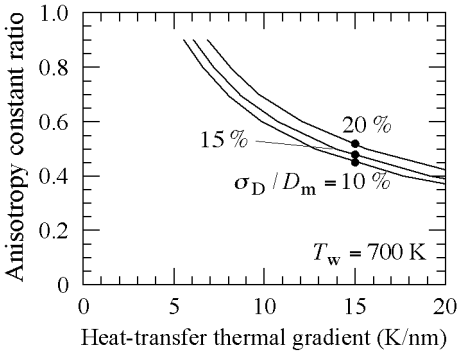

Fig. 7 Dependence of K_u/K_{bulk} on $\partial T/\partial x(y)$ at (a) T_w = 500 K[4] and (b) 700 K for various standard deviations of grain size σ_D/D_m.

On the other hand, the limiting factor is (2), (3) $\Delta T/\Delta x(y) \leq \partial T/\partial x(y)$ when (b) T_w = 700 K. ΔT of $\Delta T/\Delta x$ is determined by the statistical thermal stability factor TSF_{rec} = TSF(0.65 ns, n, σ_D, σ_K) for the writing period of 0.65 ns[3]. Figure 8 also shows the dependence of TSF_{rec} on σ_D. The TSF_{rec} increase rate is smaller than that of TSF_{10} since the probability of magnetization reversal is low even for a small size grain during a short period, *e.g.* 0.65 ns. Therefore, a large σ_D is allowable during the writing process. After writing, the medium is cooled to T_a, and then K_{um} becomes sufficiently large to hold information for 10 years even when the grain size is small.

Figure 9 shows the temperature dependence of K_{um} for T_w = 500 K and 700 K. K_u/K_{bulk} is 0.45 for both cases. $K_u(T_a)$ for T_w = 700 K is sufficiently larger than that for $K_{um}(T_a)V_m/kT_a = \mathrm{TSF}_{10}$ since the temperature difference between T_a and T_w is sufficiently large. On the other hand, $K_u(T_a)$ for T_w = 500 K is insufficient for $K_{um}(T_a)V_m/kT_a = \mathrm{TSF}_{10}$.

With conventional magnetic recording, microwave-assisted magnetic recording, and bit-patterned media, the limiting factor is $K_{um}(T_a)V_m/kT_a \geq \mathrm{TSF}_{10}$, and σ_D must be restricted to a small value. With HAMR, a relatively large σ_D is allowable when T_w is high. This is the advantage of HAMR, which utilizes the change of temperature.

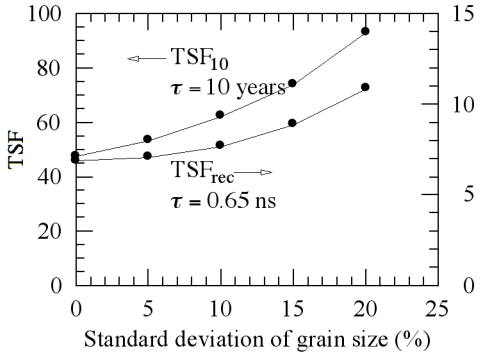

Fig. 8 Dependence of statistical thermal stability factor TSF on standard deviation of grain size σ_D/D_m for a period τ = 10 years and 0.65 ns.

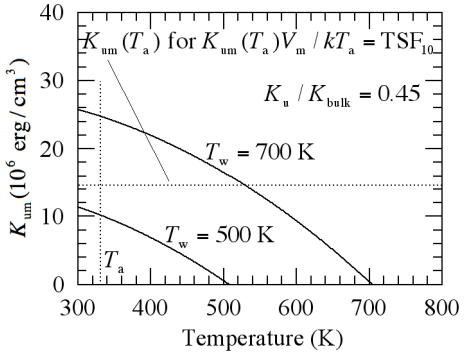

Fig. 9 Temperature dependence of K_{um} for T_w = 500 K and 700 K.

3.4 Standard deviation of anisotropy

A normal distribution was used for the K_u distribution. The calculation results for the standard deviation of the anisotropy σ_K are shown in Fig. 10. A comparison of σ_D in Fig. 7 (a) and σ_K in Fig. 10 (a) reveals that the dependence of K_u/K_{bulk} on σ_K is smaller than that on σ_D. This difference can be explained by the formula of the grain-error probability,

$$1-\exp\left(-f_0\tau\exp\left(-\mathrm{TSF}\cdot\frac{D^2}{{D_m}^2}\cdot\frac{K_u}{K_{um}}\right)\right), \quad (6)$$

where f_0 = 10^{11} s^{-1} is an attempt frequency. In the parenthesis in the formula, the variables of grain size and anisotropy are D^2 and K_u, respectively. Therefore, the dependence of K_u/K_{bulk} on σ_K is small.

As σ_K increases, K_u/K_{bulk}, shown by the filled circle in Fig. 10, is greatly increased when (a) T_w = 500 K. On the other hand, when (b) T_w = 700 K, there is little increase in K_u/K_{bulk} when σ_K is increased. The reason is the same as with the grain size distribution. Therefore, a relatively large σ_K is allowable when T_w is high, and this is also an advantage of HAMR.

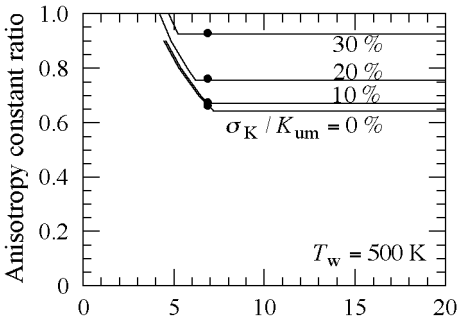

(a)

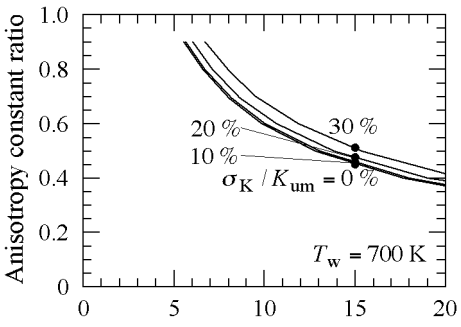

(b)

Fig. 10 Dependence of K_u/K_{bulk} on $\partial T/\partial x(y)$ at (a) T_w = 500 K and (b) 700 K for various standard deviations of anisotropy σ_K/K_{um}.

3.5 Standard deviation of Curie temperature

Next, we discuss the T_c distribution. A normal distribution was used for the standard deviations of the writing temperature σ_{Tw} and the Curie temperature σ_{Tc}. We assumed n = 1. Figure 11 shows how σ_{Tw} is calculated. The temperature at the center of the bit pitch d_B is T_w, and the temperature at the edge is $T_w \pm \Delta T_w$. Then ΔT_w is expressed as

$$\Delta T_w = \frac{\partial T}{\partial x} \cdot \frac{d_B}{2}. \qquad (7)$$

If $\Delta T_w = 3.29\sigma_{Tw}$, the bit error rate of the write error becomes 10^{-3}, that is,

$$\int_{-3.29\sigma}^{3.29\sigma} f(x)dx = 1 - 10^{-3}, \qquad (8)$$

where $f(x)$ is a normal distribution. Therefore, σ_{Tw} is expressed as

$$\sigma_{Tw} = \frac{1}{3.29} \cdot \frac{\partial T}{\partial x} \cdot \frac{d_B}{2}. \qquad (9)$$

$\sigma_{Tw} \approx \sigma_{Tc}$ is assumed, and the calculation results are summarized in Table 3. As T_w increases, $\partial T/\partial x$ increases, and then, σ_{Tc} increases. σ_{Tc}/T_c also increases despite the increase in T_c. Therefore, when T_w is high, a relatively large σ_{Tc}/T_c is allowable.

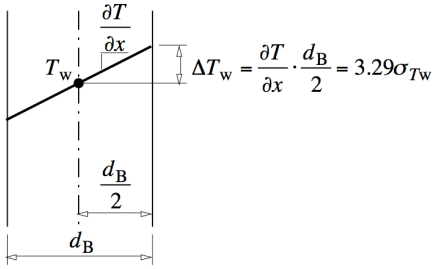

Fig. 11 Standard deviation of writing temperature σ_{Tw} for a bit error rate of 10^{-3}.

Table 3 Dependence of standard deviation of Curie temperature σ_{Tc}/T_c on writing temperature T_w.

T_w (K)	500	600	700
n (grain / bit)	1	1	1
$\partial T/\partial x$ (K / nm)	6.92	11.0	15.1
d_B (nm)	6.57	6.81	6.95
σ_{Tw} (K)	6.91	11.4	15.9
$\sigma_{Tc} \approx \sigma_{Tw}$ (K)	6.91	11.4	15.9
T_c (K)	508	606	704
σ_{Tc}/T_c (%)	1.4	1.9	2.3

3.6 Temperature dependence of anisotropy field

The temperature dependence of the magnetic properties is important in HAMR[6]. Figure 12 (a) shows the temperature dependence of the normalized anisotropy field $H_k/H_k(300\ K)$ for a low T_c = 580 K. The solid line was calculated using a mean field theory. The filled circles are experimental data for Fe-Ni-Pt reported by Thiele *et al.*[7]. The values of the experimental data are somewhat lower than those predicted by the theory. We think that this experimental behavior is a disadvantage of HAMR in terms of the writing field range for a good signal-to-noise ratio[6]. In contrast, the experimental data are well fitted to the calculation line for a high T_c = 770 K as shown in Fig. 12 (b). Since T_w must be increased to increase T_c, increasing T_w also has an advantage in terms of the temperature dependence of the anisotropy field.

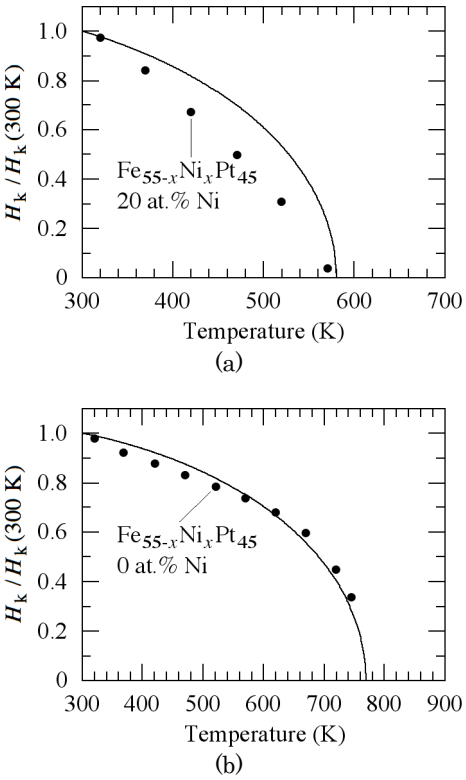

Fig. 12 Temperature dependence of normalized anisotropy field $H_k / H_k(300\ \mathrm{K})$ for (a) Curie temperature T_c = 580 K and (b) 770 K (filled circles: Fe-Ni-Pt data[7]).

4. Conclusions

We summarized the advantages of increasing the writing temperature T_w in heat-assisted magnetic recording (HAMR).

(1) Since $K_{um}(T_a)$ and $\partial T / \partial x(y)$ are increased, the anisotropy constant ratio K_u / K_{bulk} can be decreased where $K_{um}(T_a)$ is the mean anisotropy constant at the maximum working temperature T_a of the hard drive, and $\partial T / \partial x(y)$ is the heat-transfer thermal gradient calculated by a heat-transfer simulation.

(2) The K_u / K_{bulk} values are almost the same for the calculation range from the recording-layer (RL) thickness h = 6 nm to 10 nm since $\partial T / \partial x(y)$ is reduced by increasing h due to the adiabatic effect of RL. Therefore, a relatively thin RL thickness is allowable.

(3) A relatively large standard deviation of grain size σ_D is allowable since the probability of magnetization reversal is low even for small size grains during the writing period.

(4) A relatively large standard deviation of anisotropy σ_K is allowable.

(5) A relatively large standard deviation of Curie temperature σ_{Tc} is allowable since $\partial T / \partial x(y)$ is increased. σ_{Tc} / T_c also increases despite the increase in the Curie temperature T_c.

(6) For Fe-Ni-Pt films, the temperature dependence of the anisotropy field is suitable for HAMR when T_w is high.

All the above-mentioned factors are advantageous when preparing HAMR media.

Acknowledgements We acknowledge the support of the Advanced Storage Research Consortium (ASRC), Japan.

References

1) S. H. Charap, P. -L. Lu, and Y. He: *IEEE Trans. Magn.*, **33**, 978 (1997).
2) T. Kobayashi, Y. Isowaki, and Y. Fujiwara: *J. Magn. Soc. Jpn.*, **39**, 8 (2015).
3) T. Kobayashi, Y. Isowaki, and Y. Fujiwara: *J. Magn. Soc. Jpn.*, **39**, 139 (2015).
4) T. Kobayashi, Y. Isowaki, and Y. Fujiwara: to be published in *J. Magn. Soc. Jpn.*, **40**, (2016).
5) Y. Isowaki, T. Kobayashi, and Y. Fujiwara: *J. Magn. Soc. Jpn.*, **38**, 1 (2014).
6) J. -G. Zhu and H. Li: *IEEE Trans. Magn.*, **49**, 765 (2013).
7) J. -U. Thiele, K. R. Coffey, M. F. Toney, J. A. Hedstrom, and A. J. Kellock: *J. Appl. Phys.*, **91**, 6595 (2002).

Received Oct. 9, 2015; Accepted Dec. 25, 2015

J. Magn. Soc. Jpn., **40**, 35-38 (2016) <Paper>

Winding Arrangement of High-frequency Amorphous Transformers for MW-class DC-DC Converters

H. Tanaka, K. Nakamura, and O. Ichinokura

Graduate School of Engineering, Tohoku University, *6-6-05 Aoba, Aramaki, Aoba-ku, Sendai 980-8579, Japan*

Many offshore wind-power generators over MW-class are currently in operation in Europe and are now starting to be used in Japan. In order to develop large-scale offshore wind-power plants, we need to reduce the size and weight of power converters, including isolating transformers. A dc-dc converter with a high-frequency transformer is one of the best ways to reduce the size and weight. However, copper loss of the transformer due to proximity effect is a problem because the operating frequency is increased from the commercial frequency to several kHz. In this work, we investigate an interleaved winding arrangement for the high-frequency transformer. We compared the winding resistances of the interleaved and non-interleaved winding arrangements in an experiment using a test amorphous transformer and found that the interleaved winding arrangement inhibits the proximity effect and reduces the winding resistance. We designed an MW-class high-frequency amorphous transformer with the interleaved winding and demonstrated its very high efficiency.

Key words: dc-dc converter, amorphous transformer, interleaved winding, proximity effect

1. Introduction

Offshore wind-power generation is expected to substitute for conventional thermal power and nuclear power generations. In Europe, a large number of over MW-class offshore wind-power generators are already operated [1], and it has started in Japan. Such a large-scale offshore wind-power plant requires a MW-class dc-dc converter to efficiently send the generated power by high voltage direct current (HVDC) transmission system [2].

Fig. 1 shows a basic configuration of the wind-power generation system by HVDC. In the system, a permanent magnet synchronous generator (PMSG) is employed because of high power, high efficiency, and maintenance free operation. The dc-dc converter requires a MW-class transformer for isolating and boosting.

To reduce size and weight of such a large-capacity transformer, an amorphous core is employed and its operating frequency is increased from commercial frequency to several-kHz. However, it is expected that copper loss of the transformer becomes large due to proximity effect [3].

To overcome the above problem, this paper investigates an interleaved winding arrangement. First, leakage flux distribution and current density distribution of the interleaved and non-interleaved windings are compared by using finite element method (FEM). Next, frequency dependences of the winding resistance of the interleaved and non-interleaved windings are compared experimentally by using a test amorphous transformer. Finally, a MW-class amorphous transformer with the interleaved winding is designed and calculated the loss and efficiency.

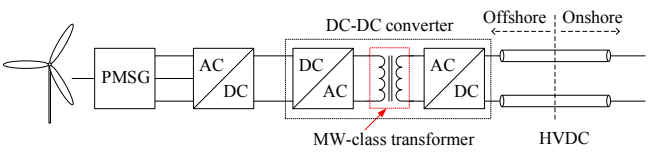

Fig. 1 Basic configuration of wind-power generation system by HVDC.

2. Comparison of the winding arrangements based on measurement and calculation

2.1 Calculated results

Fig. 2(a) illustrates shape and winding arrangement of a test amorphous transformer with the non-interleaved winding, and (b) shows with the interleaved winding. The height, width, and thickness of the transformer are 235 mm, 135 mm, and 95 mm, respectively. As shown in the figures, the winding shape is rectangular, and its size is 7 mm width by 0.8 mm thickness. The numbers of the primary and secondary windings are 96 each.

In the FEM calculation, the primary winding is excited by ideal sinusoidal current, and the secondary winding is shorted in the same way as a short-circuit test of the transformer. The electric resistivity of the primary and secondary wires is 2.52×10^{-8} Ω·m and the relative permeability of the magnetic core is 5000.

Figs. 3 and 4 indicate leakage flux density distribution around the non-interleaved and interleaved windings at an operating frequency of 3 kHz. The figures reveal that the interleaved winding arrangement can significantly reduce the leakage flux around the windings.

Figs. 5 and 6 show current density distribution of the non-interleaved and interleaved windings and their enlarged views. It is understood that the current distribution of the non-interleaved winding is non-uniform due to the proximity effect. On the other hand, the current density distribution of the interleaved

winding is uniform.

Fig. 7 indicates calculated frequency dependence of the winding resistances of the transformers with the interleaved and non-interleaved windings. It is clear that the winding resistance of the non-interleaved winding is considerably increased even though an operating frequency is below 1 kHz. On the other hand, the winding resistance of the interleaved winding is almost constant.

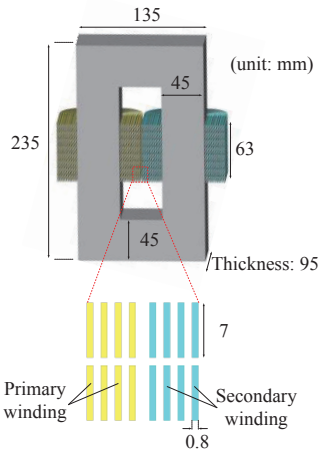

(a) Non-interleaved winding arrangement

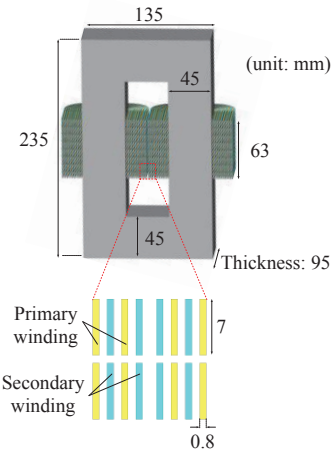

(b) Interleaved winding arrangement

Fig. 2 Shape and winding arrangement of a test amorphous transformer.

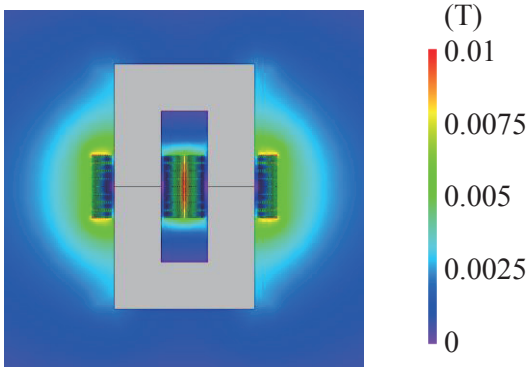

Fig. 3 Leakage flux density distribution around the non-interleaved winding (f = 3 kHz).

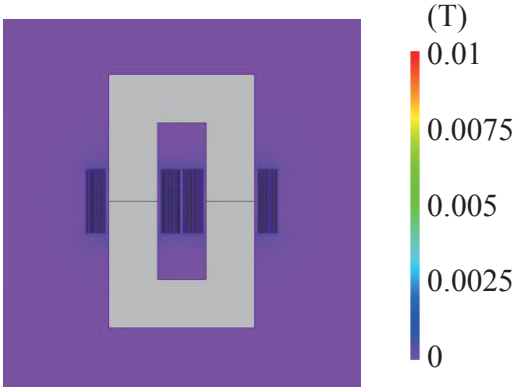

Fig. 4 Leakage flux density distribution around the interleaved winding (f = 3 kHz).

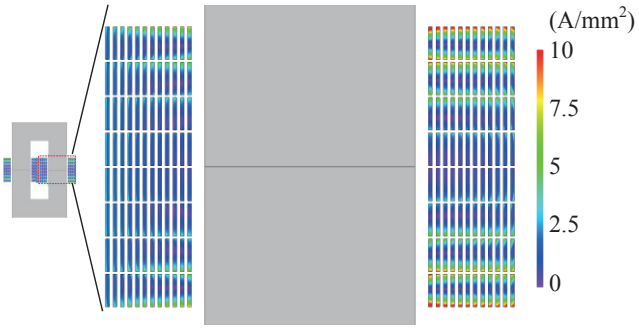

Fig. 5 Current density distribution of the non-interleaved winding and its enlarged view (f = 3 kHz).

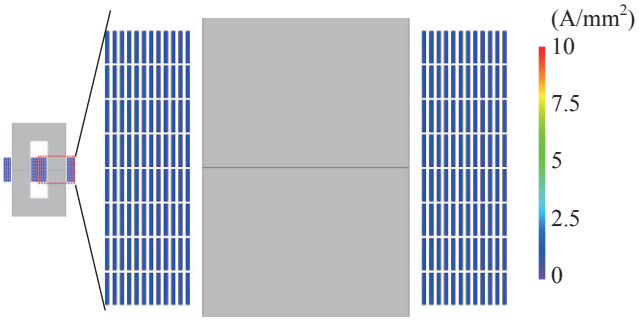

Fig. 6 Current density distribution of the interleaved winding and its enlarged view (f = 3 kHz).

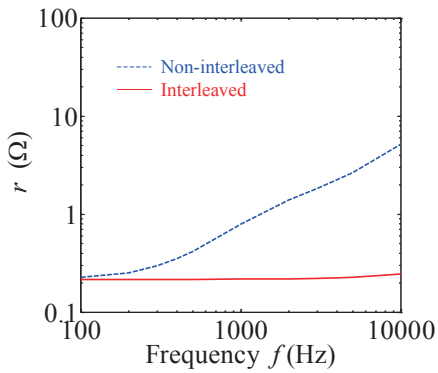

Fig. 7 Frequency dependence of the winding resistances calculated by FEM.

Fig. 8 The test amorphous transformer.

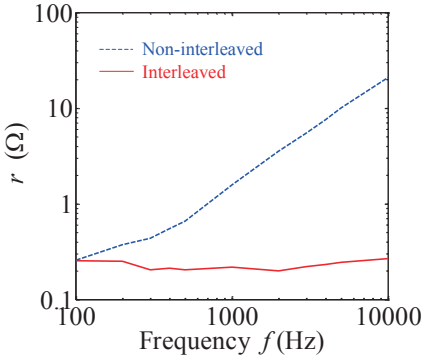

Fig. 9 Measured frequency dependence of the winding resistances.

2.2 Measured results

Fig. 8 shows an appearance of the test amorphous transformer. The shape and the winding arrangements are the same as the transformers shown in Fig. 2.

Fig. 9 indicates measured frequency dependence of the winding resistances of the transformers with the interleaved and non-interleaved windings. The figure reveals that the winding resistance of the non-interleaved winding is increased remarkably in the same manner as the calculation result shown in Fig. 7. It is proved experimentally that the interleaved winding arrangement can significantly reduce the winding resistance. The causes of error between the calculated and measured values of non-interleaved winding arrangement could be that the calculated values are obtained from the 2D-FEM.

3. Design of high-frequency amorphous transformer for MW-class dc-dc converters

3.1 Specifications of MW-class amorphous transformer

Based on the above results, a MW-class amorphous transformer with the interleaved winding is designed and compared to the transformer with the non-interleaved winding. In the design of the amorphous transformer, insulation distance of the adjacent windings is different according to the winding arrangement. The insulation distance of the non-interleaved winding arrangement is 1 mm, while the insulation distance of the interleaved winding arrangement is increased to 5 mm because the primary and secondary windings are adjacent to each other.

Table 1 shows specifications of the amorphous transformer for MW-class dc-dc converters. A turn ratio of the transformer is 10.

Fig. 10 illustrates shape and winding arrangement of the amorphous transformers for MW-class dc-dc converters, which satisfy the required specifications shown in Table 1. The height, width, and thickness of the transformer with the non-interleaved winding are 321 mm, 234 mm, and 202 mm, respectively. On the other hand, the height, width, and thickness of the transformer with the interleaved winding are 321 mm, 338 mm, and 202 mm, respectively. As shown in the figure, the winding shape is rectangular. The size of the primary winding is 100 mm width by 2.0 mm thickness, while the size of the secondary winding is 10 mm width by 2.0 mm thickness. The numbers of the primary and secondary windings are 14 and 140, respectively.

Table 1 Specifications of the amorphous transformer for MW-class dc-dc converters.

Frequency f	3 kHz
Rated power P	1.0 MW
Input voltage V_1	1.65 kV
Output voltage V_2	16.5 kV
Max. flux density B_m	1.0 T
Current density J	3 A/mm^2

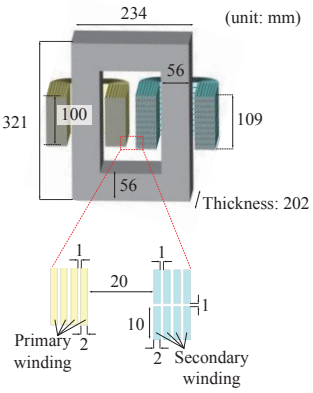

(a) Non-interleaved winding arrangement

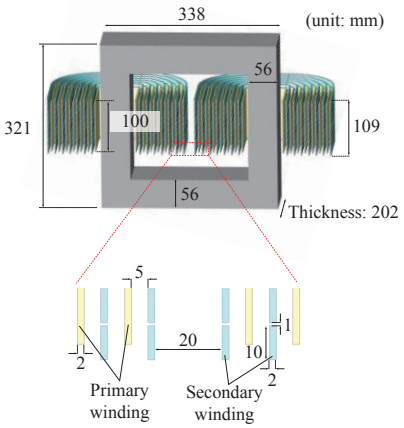

(b) Interleaved winding arrangement

Fig. 10 Shape and winding arrangement of the amorphous transformers for MW-class dc-dc converters.

3.2 Calculated results

Fig. 11 indicates calculated frequency dependence of copper losses of the MW-class transformers. In the FEM calculation, the primary winding is excited by the ideal sinusoidal current, and the secondary winding is shorted. The figure reveals that the copper loss of the non-interleaved winding is increased considerably, and that the interleaved winding arrangement can remarkably reduce the copper loss.

Table 2 shows calculated losses of the MW-class transformers. The core loss of the transformer is calculated based on the Bertotti's equation [4]:

$$W_i = A_h f B_m^2 + A_e f^2 B_m^2 + A_a f^{1.5} B_m^{1.5}, \quad (1)$$

where the frequency is f, and the maximum flux density is B_m. In (1), the first term shows dc hysteresis loss, the second term indicates classical eddy current loss, and the third term expresses anomalous eddy current loss, respectively. The parameters A_h, A_e, and A_a can be found by approximating $W_i / f - f$ curves of core material based on least-square method as shown in Fig. 12. The parameters A_h, A_e, and A_a are obtained as $A_h = 4.31 \times 10^{-3}$, $A_e = 1.81 \times 10^{-7}$, and $A_a = 6.38 \times 10^{-5}$, respectively.

It is understood from Table 2 that the interleaved winding arrangement is very useful for the high-frequency transformer of the MW-class dc-dc converters from the view point of the copper loss and the thermal design.

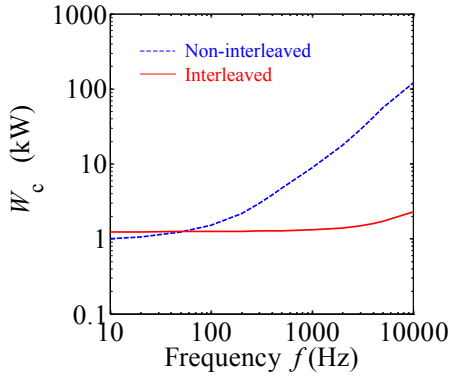

Fig. 11 Calculated frequency dependence of copper losses of the MW-class amorphous transformers.

Table 2 Calculated losses of the MW- class amorphous transformers (f = 3 kHz).

	Non-interleaved winding arrangement	Interleaved winding arrangement
Core loss W_i (kW)	1.5	1.8
Copper loss W_c (kW)	28.6	1.5
Total loss W_i+W_c (kW)	30.1	3.3
Transformer efficiency (%)	97.0	99.7

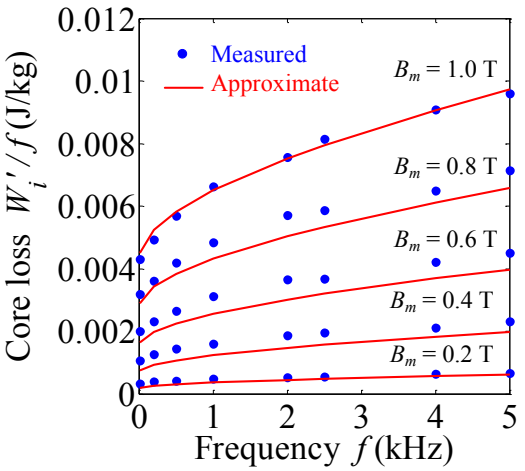

Fig. 12 W_i / f - f curves and their approximate curves of amorphous core.

4. Conclusion

This paper investigated the winding arrangement of the high-frequency amorphous transformer for MW-class dc-dc converters. By comparing the frequency dependences of the winding resistance of the interleaved and non-interleaved winding arrangements, it was clear that the interleaved winding arrangement can significantly reduce the winding resistance.

In addition, the 1.0 MW amorphous transformer with the interleaved winding was designed. It was found that the interleaved winding arrangement is very useful for the MW-class high-frequency amorphous transformer from the view point of the copper loss reduction.

This work was supported by Grant-in-Aid for JSPS Fellows (26-5193).

References

1) J. Twidell and G. Gaudiosi: Offshore Wind Power, (Multi-Science Publishing, Brentwood, 2009).
2) G. Ortiz, J. Biela, D. Bortis, J.W. Kolar, *2010 International Power Electronics Conference (IPEC 2010)*, 3212 (2010).
3) P.L. Dowell, *The Proceedings of the Institution of Electrical Engineers*, **113**, 1387 (1966).
4) G. Bertotti, *IEEE Trans. Magn.*, **24**, 621 (1988).

Received Oct 19, 2015; Accepted Dec 29, 2015

J. Magn. Soc. Jpn., **40**, 39-44 (2016) <Paper>

Reduction of Magnetic Field from Receiving Side by Separated Coil in Contactless Charging Systems for Moving Electric Vehicle

S. Aoki, F. Sato[*,**], S. Miyahara[*], H. Matsuki[*], and T. Takura[***]

Graduate School of Engineering, Tohoku Univ., *6-6-05 Aramaki-aza Aoba, Aoba-ku, Sendai, Miyagi 980-8579 Japan*

[*] Graduate School of Biomedical Engineering, Tohoku Univ., *6-6-05 Aramaki-aza Aoba, Aoba-ku, Sendai, Miyagi 980-8579 Japan*

[**] School of Engineering, Tohoku Gakuin Univ., *1-13-1 Chuo, Tagajo, Miyagi 985-8537 Japan*

[***] School of Engineering, Tohoku Institute of Tech., *35-1 Kasumi-cho, Taihaku-ku, Sendai, Miyagi 982-0831 Japan*

Two main obstacles to the wider adoption of electric vehicles are short cruising distances and long charging times. We have proposed contactless charging systems for moving electric vehicles utilizing electromagnetic induction. A problem in these systems is high level magnetic field spreading far and wide from feeding and receiving coils, which can affect electronics and human health. In our previous work, we proposed a new feeding coil shape (multipolar coil) that reduced magnetic field at a distance by over 90%. In this paper, to reduce magnetic field from the receiving coil, we newly propose a separated receiving coil and compare it with a conventional spiral receiving coil. Simulations and power transmission experiments revealed that the separated coil greatly reduced the magnetic field far from the coil and achieved high power transmission efficiency of over 80%.

Key words: Contactless charging system, Electric vehicle, Magnetic fields

1. Introduction

1.1 Contactless Charging Systems for Moving Electric Vehicles

Recently, electric vehicles (EVs) have attracted attention as environmental awareness has grown. Current EVs have problems such as short cruising distances and long charging times. These problems have prevented EVs from becoming more widespread.

To solve these problems, we have proposed contactless charging systems for moving EVs and have performed various investigations[1),2)]. These systems are able to transfer power from feeding coils in the road to a receiving coil on the underside of the EV by utilizing electromagnetic induction, which makes it possible to increase cruising distances without relying on battery capacity. Figure 1 shows a schematic diagram of a contactless charging system for moving EVs. These systems consist of an AC source, compensation circuits, feeding coils, a receiving coil, matching circuits, rectifiers, and a load (a battery or motor). The shape of the feeding coils is different from that of the receiving coil, and the size is larger in order to deliver stable magnetic coupling and transmission power[3)].

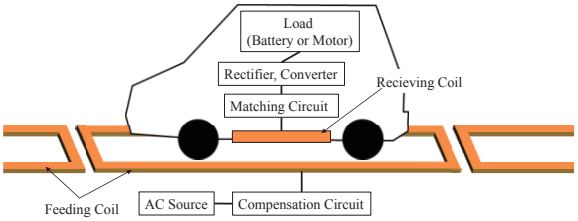

Fig. 1 Contactless charging systems for moving EVs

1.2 Electromagnetic Induction

Figure 2 shows a circuit diagram of contactless charging systems that utilize electromagnetic induction. In this figure, the resistances r_1 and r_2 are wire-wound resistors, P_{in} is input power to inverter, P_{out} is load power and the capacitances connected in series and parallel with the receiving coil are load matching capacitances. These capacitances enable power to be transmitted at maximum efficiency[1)]. The maximum efficiency, η_{max}, is determined by the coupling factor k and the quality factors Q_1 and Q_2 of the coils. Using these parameters, the performance factor α is defined as follows[1)].

$$\alpha = k^2 Q_1 Q_2 \tag{1}$$

By using α, η_{max} can be expressed as[1)]

$$\eta_{\max} = \frac{1}{1+\frac{2}{\alpha}(1+\sqrt{1+\alpha})} \tag{2}$$

The values of the load matching capacitances C_{2s} and C_{2p} can be written as[1)]

$$C_{2s} = \frac{1}{\omega r_2 \left(Q_2 - \sqrt{\frac{R}{r_2}\sqrt{1+\alpha} - (1+\alpha)}\right)} \tag{3}$$

$$C_{2p} = \frac{1}{\omega R}\sqrt{\frac{R}{r_2\sqrt{1+\alpha}} - 1} \tag{4}$$

Figure 3 shows the relationship between η_{max} and the performance factor α. High transmission efficiency is required to achieve high α.

To compensate for the power factor, the value of the

capacitance connected in series with the feeding coil is given as follows:

$$C_1 = \frac{1}{\omega^2 L_1} \tag{5}$$

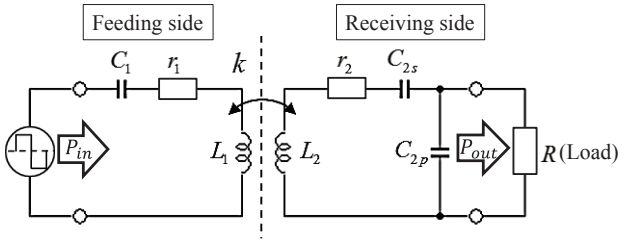

Fig. 2 Circuit diagram for contactless charging systems utilizing electromagnetic induction

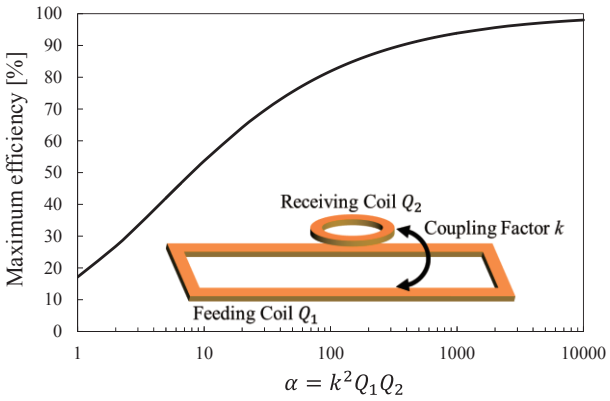

Fig. 3 Relation between α and maximum efficiency

1.3. Magnetic Field from Feeding and Receiving Coils

As shown in Fig. 1, the feeding coils are larger than the receiving coil in order to ensure stable magnetic coupling and to supply stable power along the direction of travel[3]. The size of the feeding coils in the direction of travel is 5 to 10 m. Hence, the magnetic coupling factor, k, is assumed to be less than 0.1, meaning that high-level magnetic fields are generated from the feeding and receiving coils. The magnetic field can affect electronics and human health to a distant place. It is therefore necessary to reduce the magnetic field from these coils. Many studies have investigated reduction of magnetic field from contactless charging systems[5),6)].

In previous work, we proposed a new shape of feeding coil (multipolar coil) which is able to reduce the magnetic field at a distance by over 90% compared with that of conventional rectangular coils[7)]. The multipolar coil consists of a feeding loop at the center of the coil and two loops for offsetting the magnetic field on both sides of the feeding loop as shown in Fig. 4. The loops for offsetting the magnetic field are excited in the opposite phase to the feeding loop in order to cancel out the magnetic field from the feeding loop. When the multipolar coil is used, the majority of the magnetic field from the combined feeding and receiving coil system is generated from the receiving coil. It is therefore necessary to reduce the magnetic field from the receiving coil in order to reduce the magnetic field from the overall system. In this article, we propose a new shape of receiving coil with the aim of reducing magnetic field from the receiving coil and we compare the proposed coil with a conventional spiral coil.

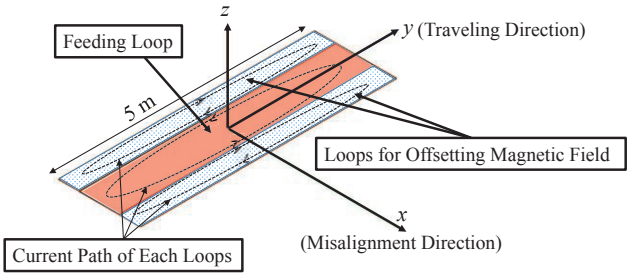

Fig. 4 Multipolar coil for reducing leakage magnetic field from the feeding coil

2. Separated Coil

2.1. Proposal of Separated Coil

We propose a new shape of coil which we call the separated coil. Figure 5 shows the structure of the separated coil. In this coil, the cross coil which has been proposed for contactless charging systems[8),9)] is split into two coils that are connected differentially. By using this configuration, the magnetic field from both coils is canceled out, reducing the magnetic field at a distance. A high coupling factor between the feeding and receiving coils can be ensured by adjusting the spacing between both coils. In this study, we define the distance between the two coils as the parameter "*Space*".

Figure 6 shows the configuration and size of the separated coil and spiral coil that were used as receiving coils in this study. The litz wire used in both coils consists of 2232 strands of 0.1 mm thick wire, and a Mn-Zn ferrite plate with a relative permeability is 2400 is placed inside the separated coil and behind the spiral coil in order to increase the inductance.

Table 1 shows the electrical properties of the separated coil and spiral coil at 100 kHz as measured with an LCR meter (E4980A, Agilent Co.) when *Space* was 0 mm, 200 mm, and 500 mm. As can be seen in the table, a high quality factor Q was confirmed as the *Space* parameter was increased because this decreased the mutual inductance and increased the

self-inductance.

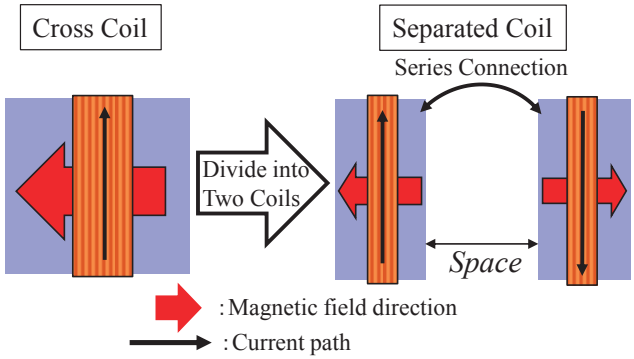

Fig. 5 Structure of separated coil

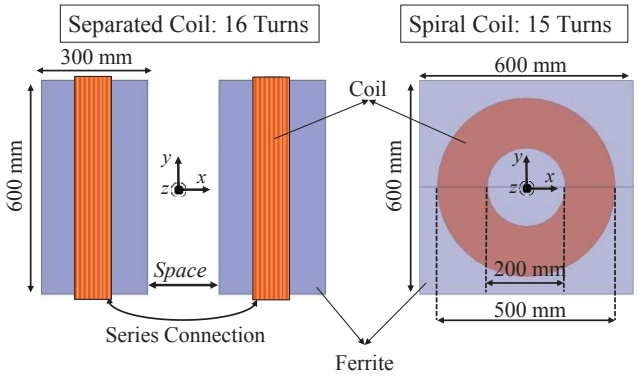

Fig. 6 Configuration and size of separated coil and spiral coil

Table1 Electrical properties of the receiving coils (frequency: 100 kHz)

Coil	Turns	*Space* [mm]	*L* [μH]	*r* [mΩ]	*Q*
Separated Coil	16	0	148	88.0	1059
		200	161	93.0	1087
		500	165	93.0	1112
Spiral Coil	15		152	113.7	840

2.2. Comparison of Magnetic Field Generated from Receiving Coils

First, in order to indicate magnetic field structures of separated coil and spiral coil, we analyzed flux lines generated from each coils. Figure 7-(a) shows the simulation models and analysis plane (*x*-*z* plane). Figure 7-(b) shows the analysis results. The excitation condition is a current of 1 A. In Fig.7 (b), we used Maxwell®2D electromagnetic field analysis software (ANSYS Co.) to analyze the flux lines and the value of vector potential. As shown in the Fig. 7-(b), the separated coils exhibit a 4-pole structure and their flux lines concentrate in near the coils compared with that of the spiral coil. As the *Space* parameter increases, the magnetic flux near the coil increases without the 4-pole structure changing. This characteristic makes it possible to reduce the magnetic field far from the coil and to increase interlinkage flux through the feeding coil and the coupling factor between the feeding coil and receiving coil.

Next, Fig. 8 shows comparison results for magnetic flux density at 10 m from the center of the coil on the *x*-, *y*-, and *z*-axes (as shown in Fig. 8-(a)). In Figure 8-(b), the value of flux density was calculated by Maxwell®3D electromagnetic field analysis software (ANSYS CO.) The excitation condition is a current of 1 A and a frequency of 100 kHz. In Fig.8-(b), the magnetic flux density far from the separated coils smaller than that from the spiral coil. The magnetic flux density from the separated coil with *Space* = 0 mm was lower by 73% on the *x*-axis, 86% on *y*-axis, and 93% on the *z*-axis. This shows that the separated coil reduces the magnetic field at a distance from the receiving coil.

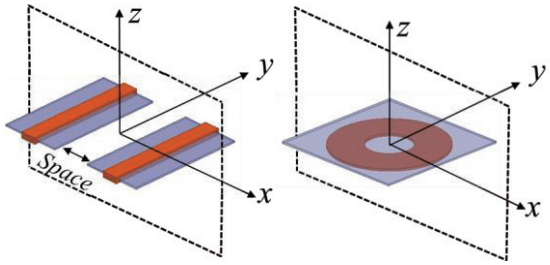

(a) Simulation models and analysis plane

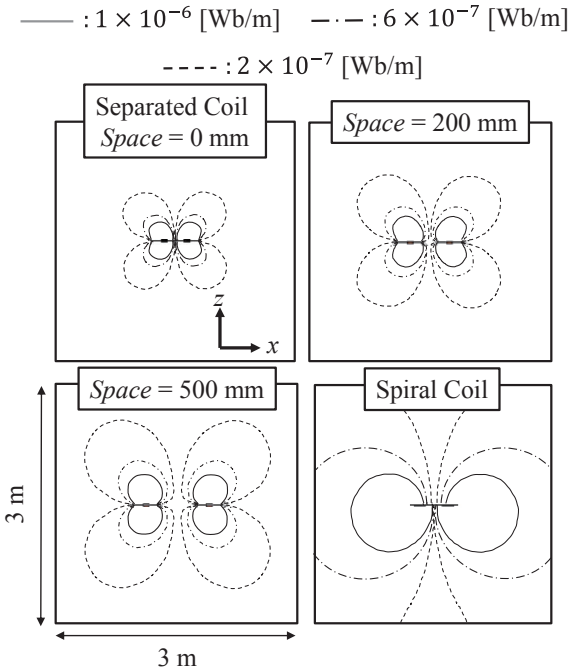

(b) Magnetic flux lines on the *x*-*z* plane

Fig. 7 Simulation models and flux lines on the *x*-*z* plane

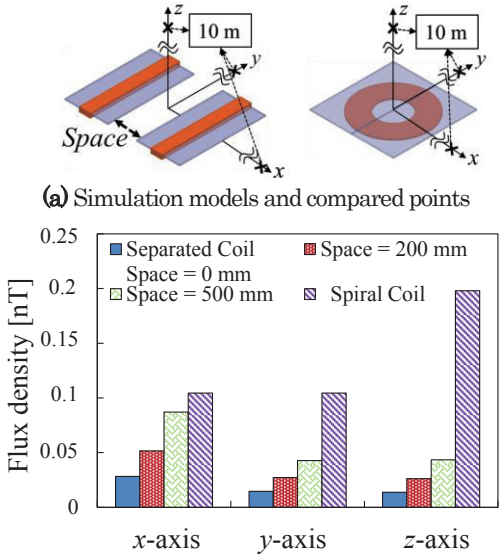

(a) Simulation models and compared points

(b) Comparison of magnetic flux density at 10 m on the *x*-, *y*-, and *z*-axis

Fig. 8 Simulation models and comparison of magnetic flux density at 10 m on the *x*-, *y*-, and *z*-axis

2.3 Coupling Coefficient between the Feeding and Receiving Coils

We measured the coupling coefficient between the feeding and receiving coils when the separated coil (*Space* = 0 mm, 200 mm, and 500 mm) and spiral coil were used as the receiving coil. Figure 9 shows the configuration of the measurement model. The feeding coil is a multipolar coil (length: 5 m; width: 1.6 m; number of loops: 1 turn). The gap between the feeding and receiving coils was set to 170 mm.

Figure 10 shows coupling factor versus location of the receiving coil along the direction of travel. The measurement results indicate that the coupling coefficient increased with increasing *Space*. This is due to an increase in the interlinkage flux as mentioned in Section 2.2, and also due to the change in relative distance between the feeding and receiving coils. The coupling coefficient was 0.035 for *Space* = 200 mm, which is comparable to the value for the spiral coil, and was 0.06 for *Space* = 500 mm. This shows that it is possible to achieve high transmission efficiency while reducing the magnetic field by using a separated coil as the receiving coil.

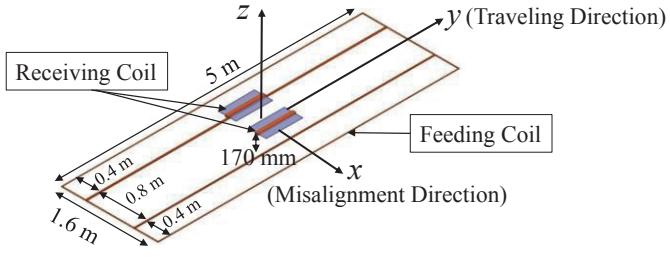

Fig. 9 Feeding and receiving coils

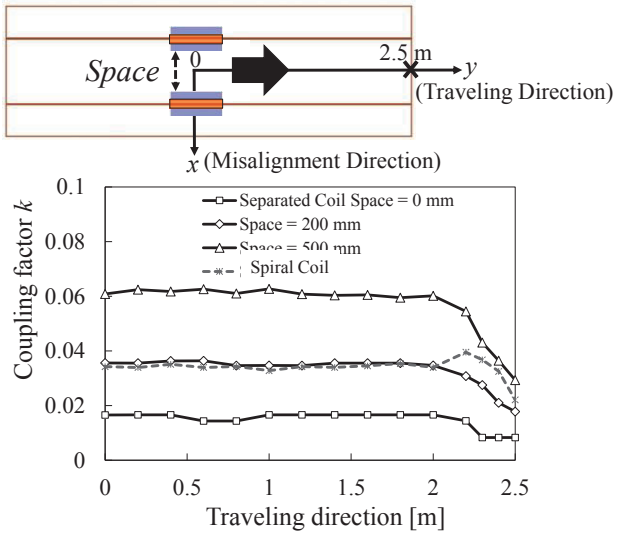

Fig. 10 Coupling factor along the direction of travel

3. Transmission Experiment and Evaluation of Magnetic Field

3.1 Transmission Experiment

We conducted transmission experiments using separated coils (*Space* = 0 mm, 200 mm, and 500 mm) and a spiral coil as the receiving coil, and measured the transmission efficiency.

The input power to the inverter was fixed at 100 W and the frequency was 100 kHz. Table 2 shows the electrical properties of the feeding coil (multipolar coil). A resistance load (10 Ω) was connected after the secondary load matching capacitances (Fig. 2).

Figure 11 shows the transmission efficiency along the direction of travel. The transmission efficiency at the center of the feeding coil was 82.1% when a separated coil with *Space* = 200 mm was used, and was 88.1% for *Space* = 500 mm. We thus confirmed that a contactless charging system with a high transmission efficiency can be constructed by using a separated coil as the receiving coil.

Table 2 Electrical properties of the feeding coil (frequency: 100 kHz)

Coil	Turns of each loop	*L* [μH]	*r* [mΩ]	*Q*
Multipolar Coil	1	46	88.1	330

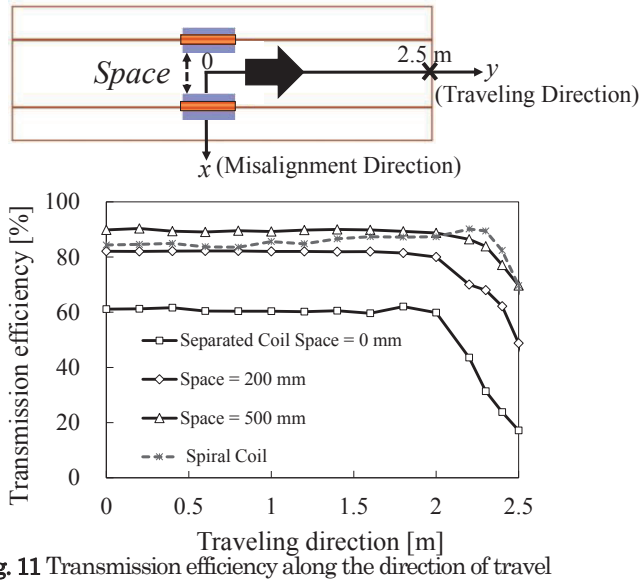

Fig. 11 Transmission efficiency along the direction of travel

3.2 Evaluation Magnetic Field from Feeding and Receiving Coils during Transmission

We analyzed the magnetic field surrounding coils during transmission and evaluated the separated coil compared to a spiral coil. Table 3 shows the estimated current values when the load power is 20 kW (by means of circuit analysis). We also analyzed the magnetic field from the feeding and receiving coils by Maxwell® 3D in terms of current values. Figure 12 shows the distribution of magnetic flux density from feeding and receiving coil. Figure12-(a) is the distribution in the *x*-direction, (b) is in the *y*-direction and (c) is in the *z*-direction. As shown in Figure12, flux density when the separated coil was used as the receiving coil is lower than spiral coil as it goes away farther from center of coil. And Figure 13-(b) shows the result of comparing the magnetic flux density at 10 m from the center of the coil on the *x*-, *y*-, and *z*-axes (as shown in Figure 13-(a)). The leakage magnetic field was reduced by 64% on the *x*-axis, 81% on the *y*-axis and 90% on the *z*-axis compared to using a spiral coil when the separated coil with *Space* = 200 mm was used as the receiving coil.

Table 3 Coil current (20 kW class)

Receiving Coil	*Space* [mm]	$I_{Feeding\_coil}$ [A]	$I_{Recieving\_coil}$ [A]
Separated Coil	0	171	159
	200	103	106
	500	72	76
Spiral Coil		118	99

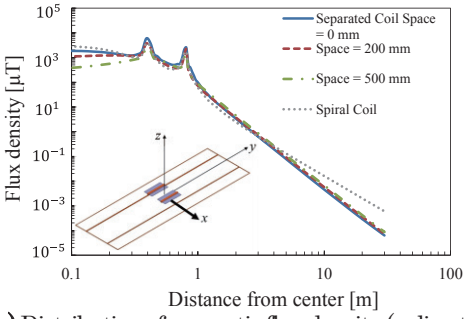

(a) Distribution of magnetic flux density (*x*-direction)

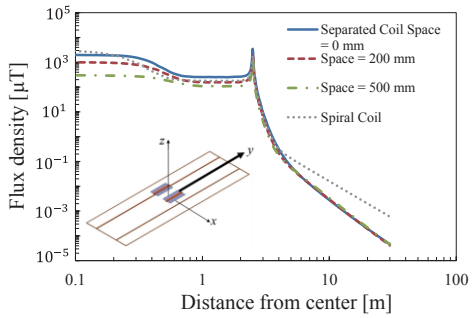

(b) Distribution of magnetic flux density (*y*-direction)

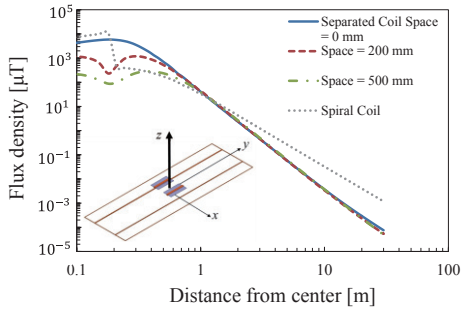

(c) Distribution of magnetic flux density (*z*-direction)

Fig. 12 Distribution of magnetic flux density from

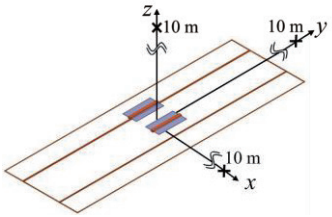

(a) Simulation model and compared points

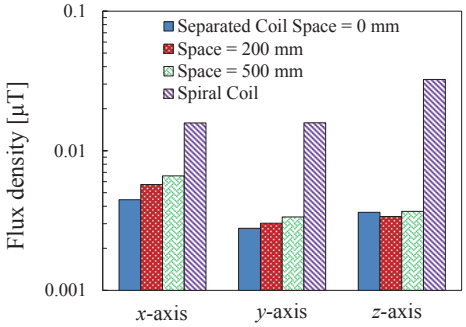

(b) Comparison of magnetic flux density (at 10 m from center of feeding coil)

Fig.13 Comparison of magnetic flux density

4. Summary

In this study, we examined the magnetic field from the receiving coil in contactless charging systems for moving EVs. This paper newly introduced the concept of the separated coil for use as the receiving coil, and compared it with a conventional spiral coil

The results of analyses and experiment showed that the magnetic field far from the coil can be reduced by approximately 90% and high transmission efficiency can be obtained by means of adjusting the *Space* parameter.

In future work, it is necessary to identify the magnetic field when the receiving coil is fitted to an EV and to reduce further magnetic field by using magnetic shielding such as aluminum sheet.

References

1) T. Takura, A. Aruga, F. Sato, T. Sato, H. Matsuki *EVTeC and APE Japan Conference Proceedings 20144028* pp.1-7 (2014)

2) T.Misawa, T.takura, F.Sato, and H.Matsuki : *IEICE Technical Report* WPT2012-33, pp13-18 (2012) (in Japanese)

3) N.Aruga, Y.Ota, Y.Imamura, S.Sato, and H. Matsuki: *J.Magn.Soc.Jpn.*, **39**, No.3, pp.121-125 (2015)

4) T.Takura, Y.Ota, K.Kato, F.Sato, and H.Matsuki *J. Magn. Soc. Jpn.,* **35**,pp. 132-135, (2011)

5) J.Shin, B.Song, S. Chung, Y.Kim, G.Jung and S.Jeon :*IEEE Wireless Power Transfer (WPT),* pp. 56-59 (2013)

6) D.Narita, T.Imura, H.Fujimoto, Y.Hori: *IEICE Technical Report* WPT2014-31, pp39-44 (2014) (in Japanese)

7) S.Aoki, F.Sato, S.Miyahara, H.Matsuki, and T.Takura:*IEICE Technical Report* WPT2015-28, pp43-48 (2015) (in Japanese)

8) Y.Kaneko, N.Ehara, T.Iwata, S.Abe, T.Yasuda, K.Ida: *IEEJ Trans. IA*, Vol.**130**,No.6,pp.734-741 (2010) (in Japanese)

9) H.Yamaguchi, T.Takura, F.Sato, and H.Matsuki: *J.Magn.Soc.Jpn.*, **38**, No.2-1 pp.33-36 (2014)

Received Oct. 16, 2015; Revised Nov. 24, 2015; Accepted Dec. 4, 2015

Journal of the Magnetics Society of Japan

Vol. 40 No. 2 (通巻第 284 号) 2016 年 3 月 1 日発行

Vol. 40 No. 2 Published March 1, 2016
by the Magnetics Society of Japan
Tokyo YWCA building Rm207, 1–8–11 Kanda surugadai, Chiyoda-ku, Tokyo 101–0062
Tel. +81–3–5281–0106 Fax. +81–3–5281–0107

Printed by JP Corporation Co., Ltd.
2–3–36, Minamikase, Saiwai-ku, Kanagawa 212–0055
Advertising agency: Kagaku Gijutsu-sha

発行：（公社）日本磁気学会 101–0062 東京都千代田区神田駿河台 1–8–11 東京YWCA会館 207 号室
製本：（株）ジェイピーコーポレーション 212–0055 神奈川県川崎市幸区南加瀬 2–3–36 Tel.（044）571–5815
広告取扱い：科学技術社 111–0052 東京都台東区柳橋 2–10–8 武田ビル 4F Tel.（03）5809–1132